Geophysical Journal International

Geophys. J. Int. (2024) **240,** 967–987
Advance Access publication 2024 November 27
GJI Seismology

https://doi.org/10.1093/gji/ggae422

Ground motion characteristics of subshear and supershear ruptures in the presence of sediment layers

Mohamed Abdelmeguid[1], Ahmed Elbanna[2,3] and Ares Rosakis[1]

[1] *Graduate Aerospace Laboratories, California Institute of Technology, Pasadena, CA 91125, USA. E-mail: meguid@caltech.edu*
[2] *Department of Civil and Environmental Engineering, University of Illinois, Urbana–Champaign, IL 61801, USA*
[3] *Beckman Institute of Advanced Science and Technology, University of Illinois, Urbana–Champaign, IL 61801, USA*

Accepted 2024 November 21. Received 2024 November 21; in original form 2024 July 18

SUMMARY

We investigate the impact of sediment layers on ground motion characteristics during subshear and supershear rupture growth. Our findings suggest that sediment layers may lead to local supershear propagation, affecting ground motion, especially in the fault parallel (FP) direction. In contrast to homogeneous material models, we find that in the presence of sediment layers, a larger fault normal (FN) compared to FP particle velocity jump, reflects shear propagation at depth but does not rule out shallow supershear propagation. Conversely, a large FP compared to FN particle velocity jump indicates supershear propagation at depth. In the presence of a shallow layer, we also uncover a non-monotonic behaviour in the sediment's influence on supershear transition and ground motion characteristics. During supershear propagation at depth we observe that sediment layers contribute to enhancing FP velocity pulses while minimally affecting the FN component. Furthermore, in the limit of global supershear propagation we identify local supersonic propagation within the sediment layers that significantly alters the velocity field around the rupture tip as observed on the free surface, creating both dilatational and shear Mach cones. In all our models with sediments we also find a significant enhancement in the fault vertical component of ground velocity. This could have particular implications for hazard assessments, such as in applications related to linear infrastructure, or a higher propensity to tsunami wave generation. Our research unravels the importance of considering heterogeneous subsurface material distribution in our physical models as they can have drastic implications on earthquake source physics.

Key words: Numerical modelling; Computational seismology; Earthquake dynamics; Earthquake ground motions; Earthquake hazards.

1 INTRODUCTION

Earthquake ruptures generate ground motions that pose significant hazards to buildings and infrastructure. In recent years, improvements in observational facilities have allowed researchers to identify several large strike-slip events. In these events, the near-source ground motion exhibits uncharacteristically large pulses. These examples include 1999 M_w7.6 Izmit (Turkey), 2002 M_w7.9 Denali (Alaska), 2016 M_w7.0 Kumamoto (Japan) and more recently the Kahramanmaraş M_w7.8 earthquake (Dunham & Archuleta 2004b; Walker & Shearer 2009; Aochi *et al.* 2011; Mello *et al.* 2014a; Kaneko & Goto 2022; Abdelmeguid *et al.* 2023; Rosakis *et al.* 2023). Such velocity pulses are usually captured only by near-fault stations. Examples include Pump station 10 for the 2002 Denali earthquake (Dunham & Archuleta 2004a; Ellsworth *et al.* 2004; Mello *et al.* 2014b), and stations TK:NAR and KO:KHMN for the magnitude 7.8 Kahramanmaraş/Pazarcik earthquake (Abdelmeguid *et al.* 2023; Rosakis *et al.* 2023). Several studies have attributed these velocity pulses to the passage of Mach fronts associated with supershear ruptures.

Supershear earthquakes are earthquakes in which the rupture speed exceeds the shear wave speed of crustal rocks C_s. Such behaviour has been observed both in the laboratory (Xia *et al.* 2004, 2005; Lu *et al.* 2010; Mello *et al.* 2010, 2014b, 2016; Rubino *et al.* 2017b) and the field (Bouchon *et al.* 2001; Ellsworth *et al.* 2004; Dunham & Archuleta 2004a; Mello *et al.* 2014b; Zeng *et al.* 2022). In a supershear rupture, the rupture propagation speed is faster than the shear wave speed. This difference in speeds results in the formation of a Mach front that moves faster than the seismic waves it generates. As previous studies have shown, the wave field generated by a propagating rupture is based on the propagation speed of the rupture front V_r relative to the shear wave speed C_s, favouring higher fault-parallel (FP) than fault-normal (FN) velocities at higher speed ratios V_r/C_s (Dunham & Archuleta 2004b, 2005; Mello *et al.*

2016; Rubino *et al.* 2020). Appendix A1 illustrates the geometrical basis for this mechanistic signature.

Recent studies revealed that supershear ruptures may be more common than previously assumed (Dunham & Archuleta 2004b; Song *et al.* 2008; Mello *et al.* 2014b; Bao *et al.* 2019, 2022; Abdelmeguid *et al.* 2023). This has led to an influx of scientific investigations on various aspects of supershear ruptures, such as the effects of Earth's free surface, stress state and material heterogeneity. The Earth's free surface significantly affects earthquake rupture dynamics. The presence of a free surface triggers free-surface-induced (FSI) supershear ruptures on strike-slip faults, facilitated by the generalized Burridge-Andrews mechanism (Kaneko & Lapusta 2010a; Hu *et al.* 2019; Xu *et al.* 2020; Hu *et al.* 2021). The role of material heterogeneity on the dynamics of supershear rupture propagation and its ground shaking has been a subject of extensive studies (Ma & Elbanna 2015; Albertini & Kammer 2017; Shlomai *et al.* 2020). Low velocity fault zones that represent damaged regions surrounding faults have been found to promote pulse-like characteristics, enhance the frequency content of the ground shaking and potentially lead to supershear transition (Duan 2008; Huang & Ampuero 2011; Ma & Elbanna 2015; Huang *et al.* 2016). Other studies have explored the role of distributed material heterogeneity on Mach cone coherence for supershear earthquakes (Vyas *et al.* 2018). Despite all the attention that supershear ruptures have garnered, one aspect that remains understudied is the interaction between supershear rupture propagation and shallow sediment layers. While a previous study explored the role of sediment layer on the supershear transition length (Xu *et al.* 2021), the near-fault ground motion characteristics associated with either local (supershear propagation within the sediment) or global supershear (supershear propagation within both the sediment and bedrock) rupture in the presence of sediment basins remain largely unexplored.

Sedimentary basins tend to form along strike-slip faults as a result of localized crustal deformations and are commonly found along major plate boundaries and mature faults (Christie-Blick & Biddle 1985; Ingersoll 1988). It has been long acknowledged that the presence of shallow layers of softer material would amplify ground motion (Jemberie & Langston 2005; Day *et al.* 2008; Frankel *et al.* 2009). An open question remains: what exactly are the characteristics of the resultant ground motion? Are the components only amplified? Or does the local heterogeneity interact with rupture propagation to alter the nature of the ground motion? Studies on the amplification of seismic records within the Mississippi Embayment have demonstrated that amplification factors can vary drastically in regions with sediment basins and local material heterogeneity from the expected factors computed using impedance contrast (Jemberie & Langston 2005). This leads to another important aspect that remains unexplored, which is how the ground motion is influenced when the rupture propagation speed is higher than the shear wave speed within the sediment, but lower than that of the bedrock. It is thus important for both the engineering and geophysical communities to explore the ground shaking that is produced by each individual scenario.

To address these knowledge gaps, we aim to investigate the near-fault ground shaking associated with surface-breaking ruptures in the presence of shallow sediment layers. We will compare the ground motion characteristics of subshear ruptures in homogeneous and layered models, with a particular focus on the effects of shallow supershear propagation. Additionally, we will explore the parameter space leading to supershear transition in layered models and examine its implications for ground motion metrics.

We will simulate several scenarios using physics-based 3-D dynamic rupture models within a rate-and-state frictional framework (Dieterich 1979; Ruina 1983; Rice & Tse 1986). Our goal is to provide insights into the potentially unique ground motion signatures that emerge in the near-fault region due to the presence of sedimentary layers and local supershear rupture propagation. Understanding these ground motion signatures may then inform the development of more accurate seismic hazard models.

In the following sections, we will describe our methodology in Section 2. In Section 3.1, we will explore the differences between a homogeneous case and a layered case with a mild material contrast. Within this model we explore two end-member cases of subshear and supershear propagation and compare the resultant ground motion characteristics. In Section 3.2 we will repeat the previous exploration for a model with stronger material contrast. In Section 3.3 we will compare key ground motion metrics for a homogeneous medium and a layered one focusing on quantities that influence the built environment response such as peak ground velocity, spectral accelerations and Fourier amplitude spectrum. In Section 4 we will discuss our results in the context of more realistic parameter distribution such as linearly varying material properties, or depth-dependent frictional variation. Furthermore, we will also explore the role of varying sediment thickness. Finally, in Section 5 we will summarize our findings.

2 MODEL SETUP

We consider a planar 2-D vertically dipping strike-slip fault embedded in a 3-D layered domain as shown in Fig. 1(a). We consider a single sediment layer of variable depth d_t km to evaluate the role of sediment depth on the ground motion. In our analysis, we only consider depth-varying stress and friction, and assume uniformity along the strike. At the rupture front, the actual rupture velocity V_r is defined as the propagation speed normal to the front and is given by $V_r = ||\nabla t_r||^{-1}$, where t_r is the time of rupture arrival computed when the slip rate exceeds a specific threshold of $0.1\,\mathrm{m\,s^{-1}}$. The horizontal rupture speed V_H is defined as $V_H = [\partial t_r/\partial x]^{-1}$.

The distribution of the depth-dependent effective normal stress is shown in Fig. 1(b) and is numerically given as $\sigma = \min[1.0 + 16.2z; 120.0]$ MPa, where z is in kilometres. The stress increases with depth due to the difference between overburden stress and the hydrostatic pore pressure and becomes constant (120.0 MPa) at depths larger than 7.4 km, due to the assumption that fluid overpressure prevents further increase of σ with depth. The existence of depth-dependent variation in stress has important ramifications in 3-D simulations as it may result in rupture front complexity (Hu *et al.* 2021). The bedrock pressure and shear wave speeds (C_p^2 and C_s^2) are chosen to be 6 and $3.46\,\mathrm{km\,s^{-1}}$, respectively. For wave speeds, the superscript $()^{1,2}$ will be used to distinguish the material properties of the sediment and bedrock, respectively. The density of both the sediment and bedrock is chosen to be $2670\,\mathrm{kg\,m^{-3}}$.

The constitutive behaviour is governed by a strong rate-weakening rate-and-state friction, in which the fault strength depends on both the rate of sliding and state evolution. The choice of a strong dynamic weakening response is motivated by experimental results that highlight a strong dependence on slip velocity at coseismic rates (Tsutsumi & Shimamoto 1997; Hirose & Shimamoto 2005; Beeler *et al.* 2008; Rubino *et al.* 2017a; Tal *et al.* 2020; Rubino *et al.* 2021, 2022). The distribution of frictional parameters along the depth is shown in Fig. 1(b).

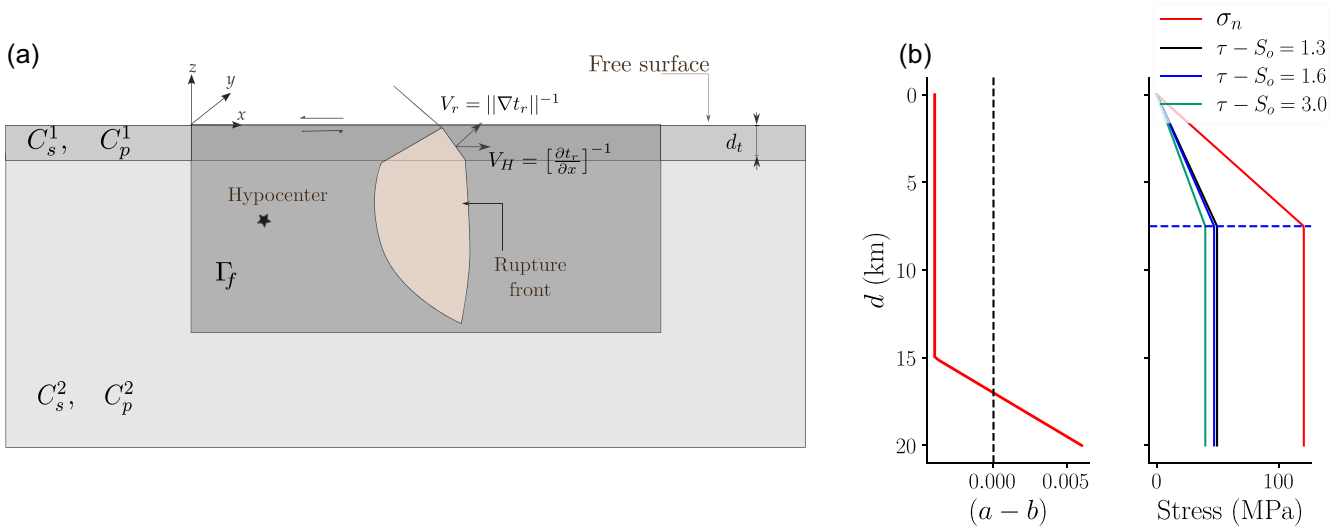

Figure 1. The 3-D dynamic rupture model setup. (a) Schematic of the simulation domain with sediment layer of depth d_t. A schematic representation of the rupture propagation along the fault surface showing the impact of the sediment layer on bending the rupture tip and altering the normal of the rupture front. The normal to the rupture front dictates the rupture speed V_r which is calculated as highlighted in the schematic. (b) The distribution of depth-variable normal stress σ, shear stress τ and frictional parameters $a - b$.

The particular form of the steady-state coefficient of friction is given as (Dunham *et al.* 2011):

$$f_{\rm ss} = f_w + \frac{f_{\rm LV} - f_w}{\left[1 + (\dot{\delta}/V_w)^8\right]^{1/8}}, \tag{1}$$

where $\dot{\delta}$ is the sliding velocity, the velocity-weakening V_w and fully weakened friction coefficient f_w are determined from laboratory experiments which suggest that $V_w \sim 0.1\ {\rm m\,s^{-1}}$ and $f_w \sim 0.2$. $f_{\rm LV}$ is the low velocity coefficient and is defined as:

$$f_{\rm LV} = f_{\rm o} - (b - a)\ln(\dot{\delta}/V_{\rm o}). \tag{2}$$

We combine this strong rate-weakening friction with the regularized version of rate-and-state friction, where the friction coefficient is expressed as:

$$f(V, \Psi) = a{\rm asinh}\left(\frac{\dot{\delta}}{2V_{\rm o}} e^{\frac{\Psi}{a}}\right) \tag{3}$$

The state variable Ψ evolves according to an evolution equation:

$$\frac{{\rm d}\Psi}{{\rm d}t} = -\frac{\dot{\delta}}{L}\left[\Psi - \Psi_{\rm ss}(\dot{\delta})\right], \quad \Psi_{\rm ss} = a\ln\left\{\frac{2V_{\rm o}}{\dot{\delta}}\sinh\left[\frac{f_{\rm ss}(\dot{\delta})}{a}\right]\right\}. \tag{4}$$

The ruptures are nucleated by artificially forcing failure in a circular region (radius = 3 km) on the faults at depth d_H until spontaneous rupture propagation occurs. The perturbation in shear stress is mathematically smooth in both space and time and is conducted by smoothly increasing the shear stress within the circular patch over a time period $t_{\rm rise}$ as described in SCEC benchmark TPV-103.

The assumed variation of frictional parameters $a - b$ with depth is shown in Fig. 1. The seismogenic zone extends from 0 to 15 km. The closer the initial shear stress state on the fault to the interface strength, the more favourable the supershear transition becomes. This notion is captured by the fault strength term $\mathcal{S}$ which quantifies the ratio of strength excess to dynamic stress drop $\mathcal{S} = (\tau_p - \tau_{\rm o})/(\tau_{\rm o} - \tau_r)$ (Andrews 1976; Das & Aki 1977). Lower values of $\mathcal{S}$ have been shown to favour shorter supershear transition length for generalized Burridge Andrews mechanism (Dunham 2007; Rosakis *et al.* 2007), and faster supershear saturation of the seismogenic zone for free-surface-induced supershear transition (Kaneko & Lapusta 2010b; Hu *et al.* 2021). This is because the transition length to supershear L_T is proportional to $L_T \propto \mathcal{S}L_f$, where L_f is the frictional length scale obtained from the frictional law (Dunham 2007). In our models, L_f is kept constant and only $\mathcal{S}$ is changed. Within rate-and-state friction, there are no well-defined a priori estimates for τ_p and τ_r. However, similar to Dunham et al. (2011), we obtain estimates for the peak strength (τ_p) and residual strength (τ_r), which we can later adjust given knowledge of the slip rate:

$$\tau_p \approx \sigma_n\left[a\ln(\dot{\delta}_{\rm co}/V_{\rm o}) + \Psi_{\rm o}\right], \qquad \tau_r \approx \sigma_n\left[f_{\rm ss}(\dot{\delta}_{\rm co})\right]. \tag{5}$$

Here, $\dot{\delta}_{\rm co}$ is the co-seismic slip velocity, assumed to be $\sim 10\ {\rm m\,s^{-1}}$, which is consistent with observed slip velocities during dynamic rupture simulations. In our study, we fix the value of the initial peak friction coefficient (given as τ_p/σ_n) to be ~ 0.72 for all simulations by setting $\Psi_{\rm o} = 0.56$. We then vary the $\mathcal{S}_{\rm o}$ parameter, computed using τ_p and τ_r, in our simulations by changing the background stress $\tau_{\rm o}$.

All the simulations in this work are conducted using an open-source software DRDG3D, which was developed by Zhang et al. (2023) for dynamic rupture modelling. DRDG3D adopts an upwind/central mixed flux scheme, which removes numerically generated artificial oscillations. The numerical efficiency and accuracy of DRDG3D are documented in Zhang *et al.* (2023) including verification with community developed Southern California Earthquake Center (SCEC) benchmarks.

3 RESULTS

In this study we are interested in understanding the ground motion characteristics of subshear and supershear ruptures in the presence of a shallow sediment layer. We will explore how those characteristics change with varying material contrast C_s^1/C_s^2, the depth of the sedimentary layer and the initial value of the strength parameter $\mathcal{S}_{\rm o}$. To focus on the effect of the sediment in this initial study, we will primarily consider a single sediment layer on top of a homogeneous half-space. We consider two contrast ratios $C_{s,p}^1/C_{s,p}^2$

Table 1. The different models considered in this study with varying sediment material properties, depth and initial stress state.

	Contrast	$\mathcal{S}_o$	d_t
Homogeneous models	$C_p^1 = C_p^2, C_s^1 = C_s^2$		
H-1		3	
H-2		1.6	
H-3		1.3	
Mild contrast models	$C_p^1 = 0.7C_p^2, C_s^1 = 0.7C_s^2$		
A-1		3	2
A-1*		3	5
A-2		1.6	2
A-2*		1.6	5
A-3		1.3	2
Strong contrast models	$C_p^1 = 0.5C_p^2, C_s^1 = 0.5C_s^2$		
B-1		3	2
B-1*		3	5
B-2		1.6	2
B-2*		1.6	5
General models			
LVS-1	Linear velocity structure (Güvercin *et al.* 2022)	3	varies
LVS-2	Linear velocity structure (Güvercin *et al.* 2022)	1.6	varies
A-1^{VS}	$C_p^1 = 0.7C_p^2, C_s^1 = 0.7C_s^2$	3	2
A-2^{VS}	$C_p^1 = 0.7C_p^2, C_s^1 = 0.7C_s^2$	1.6	2

^{VS} superscript VS indicates a model with a velocity-strengthening portion near the free surface.

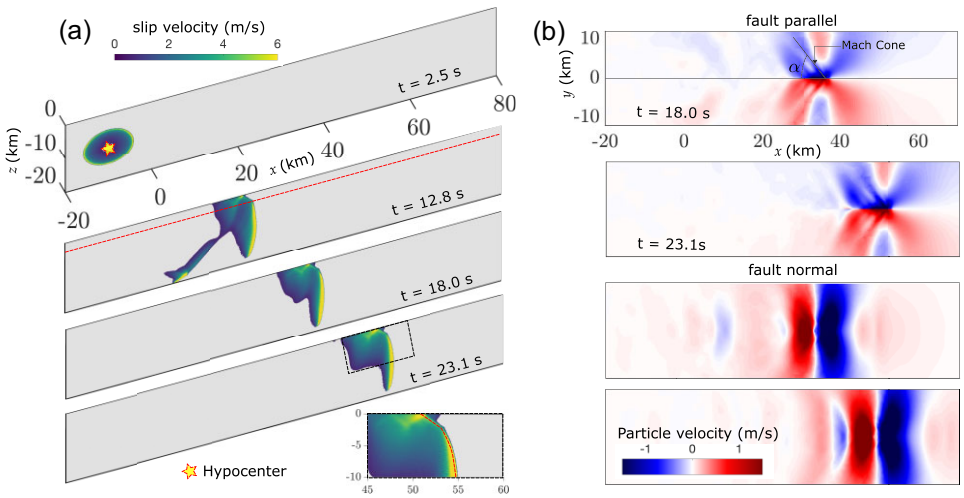

Figure 2. The role of sediment layer contrast in altering rupture propagation and ground motion characteristics for Model A-1. (a) snapshots of the rupture propagation at different times ($t = 2.5$, 12.8, 18.0 and 23.1 s). (b) Contours of the fault-parallel and fault-normal particle velocity wave-field within near field of the fault at later stages of rupture propagation ($t = 18.0$ s, and $t = 23.1$ s).

equal to 70 per cent and 50 per cent. Throughout the study, $C_{s,p}^2$ remains fixed while we vary $C_{s,p}^1$. Within each contrast ratio, we consider end member cases of the strength parameter $\mathcal{S}_o = 3$ and $\mathcal{S}_o = 1.6$. Finally, we will study the influence of sediment layers on key ground motion metrics by focusing on two models, one that is subshear $\mathcal{S}_o = 3$ and one that is supershear $\mathcal{S}_o = 1.3$. We chose a slightly smaller $\mathcal{S}_o$ to guarantee rapid supershear transition in both the homogeneous and the sediment models. A summary of all the models considered in this study is provided in Table 1.

3.1 Mild material contrast $C_{s,p}^1 = 0.7\,C_{s,p}^2$

Our starting point is a case with a mild shear and pressure wave speed contrast between the bedrock and the sediment. The depth of the sediment is chosen as $d_t = 2$ km. We will refer to this Model as A.

3.1.1 Large fault initial fault strength ratio $\mathcal{S}_o = 3$ (A-1):

In Fig. 2(a) we show snapshots of the rupture propagation. The rupture nucleates within the overstressed patch, then expands until it saturates the seismogenic zone, and proceeds to propagate along the x-direction. The rupture front bends within the sediment layer due to the lower wave speeds in that medium (as shown in the zoomed-in snapshot). This results in a change in the rupture front speed V_r which is computed based on the normal to the rupture front. At later times between $t = 18.0$ and 23.1 s, the rupture propagates steadily with an identical slip rate profile. Based on propagation distances (~ 15 km) within the last two snapshots (5.1 s), the rupture

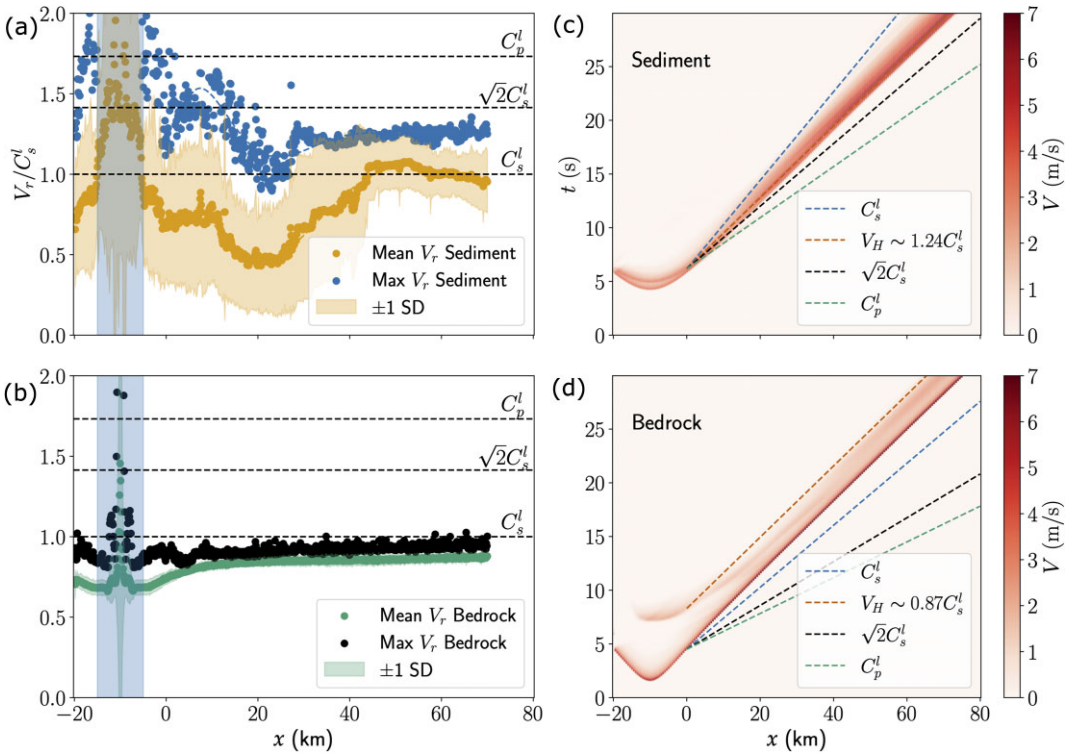

Figure 3. The rupture propagation speeds in Model A-1 (a–b) Mean and maximum rupture propagation speed V_r within both the sediment and the bedrock. The shaded area represents the nucleation site of the rupture. (c–d) Spatiotemporal slip rate distribution at depth 1 and 7.5 km, respectively, to highlight local horizontal propagation speed V_H relative to local characteristics speeds C_s^l, C_p^l and $\sqrt{2}C_s^l$.

propagation speed is $V_r = 3\,\mathrm{km\,s^{-1}}$, which is indeed 'subshear' based on the bedrock shear wave speed.

The resultant near-fault (< 12 km away from the source) particle velocity field generated by this propagation is shown in Fig. 2(b). We show the fault-parallel (FP) particle velocity wave field at times $t = 18.0$ and 23.1 s, respectively, after rupture nucleation. We observe the emergence of a Mach cone structure within the velocity field near the rupture tip. The emergence of the Mach cone is a signature of supershear rupture propagation. As mentioned earlier, the rupture is subshear within the bedrock, so the emergence of a Mach cone is attributed to local supershear propagation within the sediment. The Mach cone has an angle $\alpha \approx 52^\circ$. Despite being supershear, a Mach cone angle $\alpha_s > 45^\circ$ indicates a sub-Eshelby propagation speed. Sub-Eshelby propagation speed is characterized by a propagation speed of V_r, $V_H < \sqrt{2}C_s$. We note here that some literature refers to rupture propagation between C_s and $\sqrt{2}C_s$ as unstable supershear propagation (Burridge 1973; Andrews 1976; Bhat *et al.* 2004; Rosakis *et al.* 2007), but that is based on 2-D analyses and does not extend to 3-D propagation in a heterogeneous media or with complex fault geometry (Weng & Ampuero 2020). Furthermore, sub-Eshelby propagation has been observed in the field (Bao *et al.* 2019). Because of geometrical considerations, supershear ruptures propagating below the Eshelby speed *do not* have a fault-parallel (FP) particle velocity jump that is larger than the fault-normal (FN) particle velocity jump. In subsequent discussions, we will correlate the Mach cone angle with the horizontal rupture velocity V_H rather than the actual rupture speed within the sediment V_r. This is because the structure of the Mach cone at the free surface depends on the stress field generated by the rupture tip on the free surface, which is propagating at V_H. This is consistent with an earlier study by Hu et al. (2021), which also found that the Mach cone angle depends on the 1-D horizontal V_H speed rather than V_r (Hu *et al.* 2021). Examining the fault-normal velocity wave field shown in Fig. 2(b) at different times, we observe the characteristic 'butterfly' structure associated with subshear propagation.

The emergence of the Mach cone within the FP component can be explained by examining the rupture propagation speeds within both the sediment layer and the bedrock, as shown in Fig. 3. In Fig. 3(a), the mean and maximum values of the rupture speed V_r within the sediment layer are plotted. In the shaded region which coincides with the hypocentral location, the rupture speed exceeds the Eshelby speed ($\sqrt{2}C_s^l$). This is due to a geometric effect that accelerates the rupture propagation speed to satisfy the boundary condition at the instance the rupture front encounters the free surface. We observe a strong scatter in the rupture propagation speed within the sediment layer for the fault segment given by $0 < x < 50$ km. As the rupture propagates further, $x > 50$ km, the scatter decreases. More importantly, both the mean and maximum values of V_r exceed the shear wave speed of the sediment layer at certain points during the rupture propagation. This increase in rupture propagation speed relative to the local wave speed explains the emergence of the Mach cone at the free surface. Both quantities stay below the local Eshelby speed which is consistent with $\alpha > 45^\circ$ seen in Fig. 2(b). Within the bedrock, as shown in Fig. 3(b), both the maximum and mean V_r stay below the shear wave speed of the bedrock. This is consistent with the subshear rupture propagation observed in Fig. 2(a).

The horizontal propagation speed V_H is tracked by plotting the spatiotemporal evolution of the slip pulse within the sediment at $z = -1$ km and bedrock at $z = -7.5$ km (Figs 3c and d). In Fig. 3(c), we estimate $V_H \sim 1.24C_s^l$, which is larger than the shear wave speed but smaller than the Eshelby speed. The supershear V_H further justifies the emergence of Mach cones at the free surface. Within

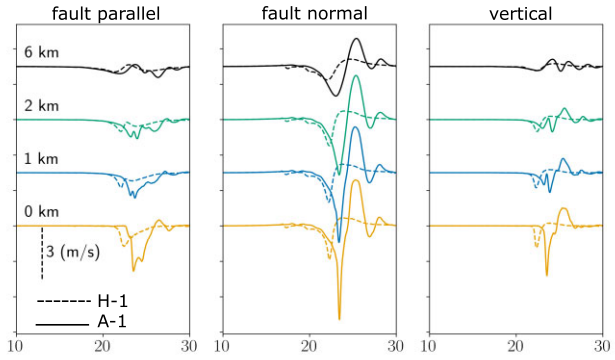

Figure 4. The role of sediment layer contrast in altering synthetic ground motion characteristics for Model A-1 (a) Fault-parallel (FP), (b) fault-normal (FN) and (c) vertical velocity time histories at four different sites. Sites are located at 50 km along strike and at distances (0^+, 1, 2, 6) along the fault perpendicular direction.

the bedrock shown in Fig. 3(d), we estimate $V_H \sim 0.87C_s^l$, which is still subshear.

With knowledge of rupture speeds, we can independently estimate the Mach cone angle α. Geometrically, the angle of the Mach cone is defined through the propagation speed as $\alpha = \sin^{-1}(C_s^l/V_H)$. Here, we use V_H because, as discussed earlier, V_H correlates better with free surface Mach cone when $V_r \neq V_H$. The rupture at depth, which is subshear, propagates with a speed $V_H \sim 0.87C_s^2$. For the given contrast, we predict the angle of the Mach cone as $\alpha = \sin^{-1}(0.7/0.87) = 54.5^\circ$, which is indeed very close to the observed angle of 52° at the free surface. Note here that we can also use $V_H = 1.24C_s^l$ directly to obtain the same solution. The difference is merely the scaling by the contrast ratio. This interchangeability implies the horizontal rupture speed is constant with depth, which is also consistent with the unchanged curvature of the rupture front seen in Fig. 2(a) once the rupture saturates the seismogenic zone at $t > 12.8$ s. This observation indicates that measurements of the horizontal rupture speed V_H at the free surface are indicative of the rupture speed V_r at larger seismogenic depth. Accordingly, assuming continuous propagation in heterogeneous media, if we measure the rupture speeds on the surface using rupture phase tracking (which typically tracks horizontal rupture speeds), we can readily extrapolate to identify rupture speed at depth by using appropriate wave speed conversion.

In Fig. 4, we plot the synthetic ground motion records for several stations located at $x = 50$ km along strike and at multiple distances along the fault perpendicular direction ($y = 0^+$, 1, 2, 6). In the very near field < 2 km, we observe that amplification occurs in all three velocity components for the model with sediment (shown as solid line) in comparison to the homogeneous model (shown as the dashed black line). At distances larger than 6 km, the extent of amplification for the fault-normal (FN) component is larger than the fault-parallel (FP) and the vertical component.

To understand the nature of the ground motion amplification, we examine the possible sources that contribute to it:

(i) Amplification may occur due to wave conversion at the interface between the bedrock and the sediment. These conversions can lead to constructive interference and amplification of seismic waves, increasing the amplitude of ground motions recorded during the earthquake. Within the near-fault velocity field, wave conversion will have a relatively small contribution due to the low contrast ratio between the bedrock and sediment. Wave conversion will not explain a three times increase in the component's amplitude in the near-fault records (Aki & Richards 2002). At distances far away from the source, we expect such conversion to be more obvious.

(ii) Rupture propagation within a softer sediment layer will enhance slip rate, which will consequently result in higher ground particle velocities. The steady-state velocity field **v**, under 2-D plane strain conditions, may be represented by Mello *et al.* (2014b):

$$\mathbf{v}\left(\frac{x}{L}, \frac{y}{L}\right) = \hat{v}_0 \mathcal{F}\left(\tfrac{x}{L}, \tfrac{y}{L}, \tfrac{R}{L}, \tfrac{V_r}{C_s}\right), \tag{6}$$

where $\hat{v}_0 = C_s \dfrac{(\tau_p - \tau_r)}{\mu}$

Here, μ is the shear modulus, and in eq. (6) the amplitude of the velocity field given by $\hat{v}_0$ is $\propto 1/\sqrt{\mu}$. This proportionality implies that if the material is softer (i.e. lower μ), the amplitude of the velocity field will be higher, assuming that the ratio V_r/C_s remains constant. The role of V_r/C_s will be discussed in the subsequent point.

(iii) Near-fault amplification associated with rupture tip propagation speed. The stress concentration factor and the resulting stress field for a dynamically propagating slip pulse depend on the ratio of the rupture speed to the local characteristic wave speeds. We can observe this dependence within eq. (6) in the term $\mathcal{F}$. Since the rupture is propagating at the same V_H within the sediment and bedrock but the local wave speed is lower in the sediment, that ratio thus increases. This increase explains the emergence of the Mach cone seen in Fig. 2. Furthermore, this increase in the rupture speed ratio changes the stress field generated near the rupture tip, potentially amplifying or dampening the ground motion.

In subsequent sections, we will explore the role of the third contribution further.

3.1.2 *Small fault strength ratio $\mathcal{S}_o = 1.6$ (A-2):*

Next, we consider a case with a fault strength ratio $\mathcal{S}_o = 1.6$. This smaller choice of $\mathcal{S}_o$ favours the transition to supershear rupture speeds in a homogeneous model (shown in Fig. A2) and within the bedrock for a model with sediment layer. We will refer to this as Model A-2.

In Fig. 5(a) we show snapshots of the slip velocity at times $t = 2.5$, 10.2 and 18 s, respectively. At $t = 10.2$ s we observe the emergence of a secondary crack ahead of the rupture tip. This secondary crack then becomes the leading rupture tip propagating at a speed that exceeds the shear wave speed within both the sediment and the bedrock. To highlight this transition, we plot the propagation speed V_r normalized by the local shear wave speed in Fig. 5(b). We observe that the rupture transitions to supershear speed $V_r/C_s^l > 1$ within both the bedrock and the sediment. Furthermore, we observe that the normalized rupture speed is higher within the sediment versus the bedrock. Compared to the homogeneous case (shown in Fig. A2), for model A-2 we observe that the transition to supershear occurs much earlier, which implies that the sediment assisted in the supershear transition. This is potentially possible due to the heterogeneous P-SV conversion at both the free surface as well as the bedrock–sediment interface (Kaneko & Lapusta 2010b; Xu *et al.* 2021).

Fig. 5(c) illustrates the particle velocity wave field for Model A-2. Within the FP component, we observe two distinct Mach cone signatures associated with (a) global supershear propagation (referring to supershear in both sediment and bedrock) with a Mach cone

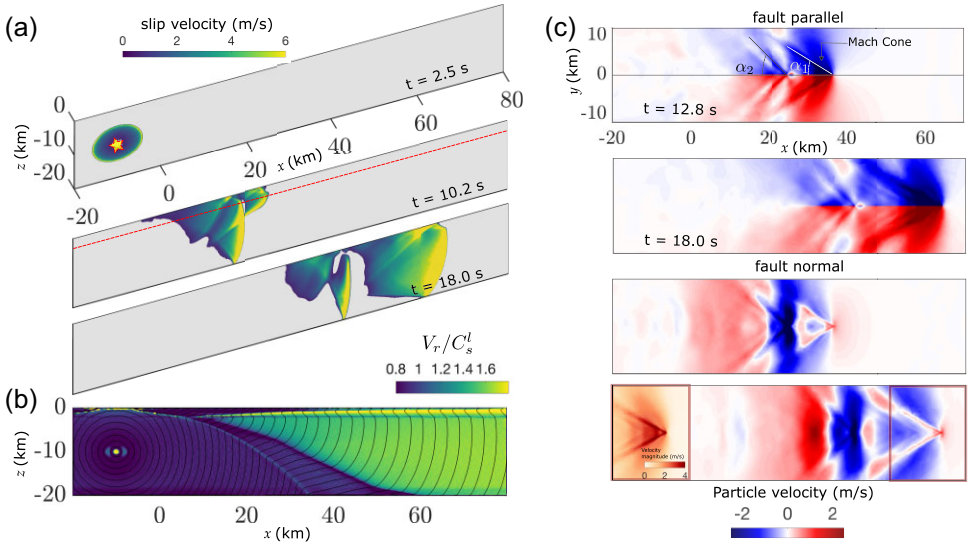

Figure 5. The role of sediment layer contrast in altering rupture propagation and ground motion characteristics for Model A-2. (a) snapshots of the rupture propagation at different times ($t = 2.5$, 10.2 and 18.0 s). (b) Contour of the normalized rupture speed V_r/C_s^l. (c) Contours of the fault-parallel and fault-normal particle velocity wave-field within near field of the fault at later stages of rupture propagation ($t = 12.8$ s and $t = 18.0$ s). Zoomed figure in last panel shows the particle velocity magnitude near the rupture tip at $t = 18.0$ s to highlight the structure of the Mach cone.

angle α_1, and (b) local supershear propagation within the trailing subshear signal which has a Mach cone angle α_2. The difference in angles is because the lead tip and the trailing one are propagating at different speeds relative to the local wave speeds. We further note that α_2 observed in Model A-2 is smaller than the α observed in Model A-1 despite both being associated with a subshear rupture at depth. This is due to the trailing Rayleigh propagating at speeds faster than that of the subshear rupture in Model A-1.

The FN component undergoes a minor change at the leading rupture tip which is propagating in both the sediment layer and the bedrock at supershear speed. This is a typical signature of supershear propagation when the rupture speed exceeds the Eshelby speed, as illustrated graphically in Fig. A2. As the rupture accelerates, the Mach cone angle α decreases and, consequently, the FN velocity perturbation carried by the Mach cone also decreases. The primary velocity pulse in the FN arrives at a later time with the trailing Rayleigh signature. We also note that the local supershear propagation in conjunction with wave reflections alters the form of the FN component relative to what is observed in Fig. 2(b).

The rupture propagation speed characteristics are shown in Fig. 6. We observe that the mean V_r within both the sediment and the bedrock exceed the Eshelby speed. Interestingly, the maximum V_r in the sediment, as shown in Fig. 6(a), exceed the local pressure wave speed C_p^l. That is not the case for the bedrock as shown in Fig. 6(b). The slip pulse propagation speeds V_H is estimated in Figs 6(c)–(d) to be $\sim 2.27C_s^l$ within the sediment and $\sim 1.6C_s^l$ with in the bedrock. Note, that the difference is due to scaling of C_s^l. Similar to Model A-1 this implies that V_H is the same with the bedrock and the sediment. The observation of similar V_H within the sediment and the bedrock is purely geometric. It emerges because for the rupture front to retain its curvature after saturating the seismogenic zone (steady state), the horizontal rupture speed at the free surface has to match the rupture speed at the interface between the bedrock and the sediment. It is important to emphasize that there is no physical justification for the rupture front curvature to change within the sediment layer, since locally the material is homogeneous, the stress field varies linearly and the propagation path is unhindered.

This *apparent* supersonic propagation driven by the rupture process at depth in conjunction with the local supershear propagation within the sediment layer led to multiple Mach cones observed within the velocity field shown in Fig. 5(c). We also observe that the trailing Rayleigh pulse is propagating at speeds slightly below the local Eshebly speed which explains the wider Mach cone angle seen in Fig. 4(b). At a depth of 7.5 km within the bedrock, a leading slip pulse is observed propagating at supershear speed relative to the local speeds. Furthermore, at depth 1, and 7.5 km we observe that the lead slip pulse propagating horizontally at the same speed V_H. This is similar to model A-1 where the speed within the sediment is directly equivalent to the speed at depth.

In Fig. 7, we plot synthetic velocity field records for stations located at $x = 50$ km along strike and at multiple distances in the fault perpendicular direction ($y = 0^+, 1, 2, 6$). Within the synthetic near-fault records, we observe larger fault-parallel (FP) than fault-normal (FN) velocity jumps associated with the leading rupture tip. *This implies that 2-D conclusions regarding velocity jumps hold true in the case of the global supershear condition, even in the presence of material heterogeneity.* At later times, we observe a secondary pulse associated with the trailing Rayleigh signal and the local supershear. In the secondary pulse, the FN component dominates the FP component. The fault-normal component shows a clear lack of amplification compared to the homogeneous case. It is also worth noting that the FN component is smaller than that observed in Model A-1. In the vertical component V_z, we observe a substantially large amplification that is absent in the homogeneous case, arriving with the leading rupture tip.

In Fig. 4, for Model A-1, we observe a strong amplification of the FN component relative to the homogeneous case. However, for Model A-2 shown in Fig. 7, there is almost no amplification for either the leading rupture field or the trailing one. To better understand this observation, we study the steady-state characteristics of a crack propagating at supershear speed. The approximation of a

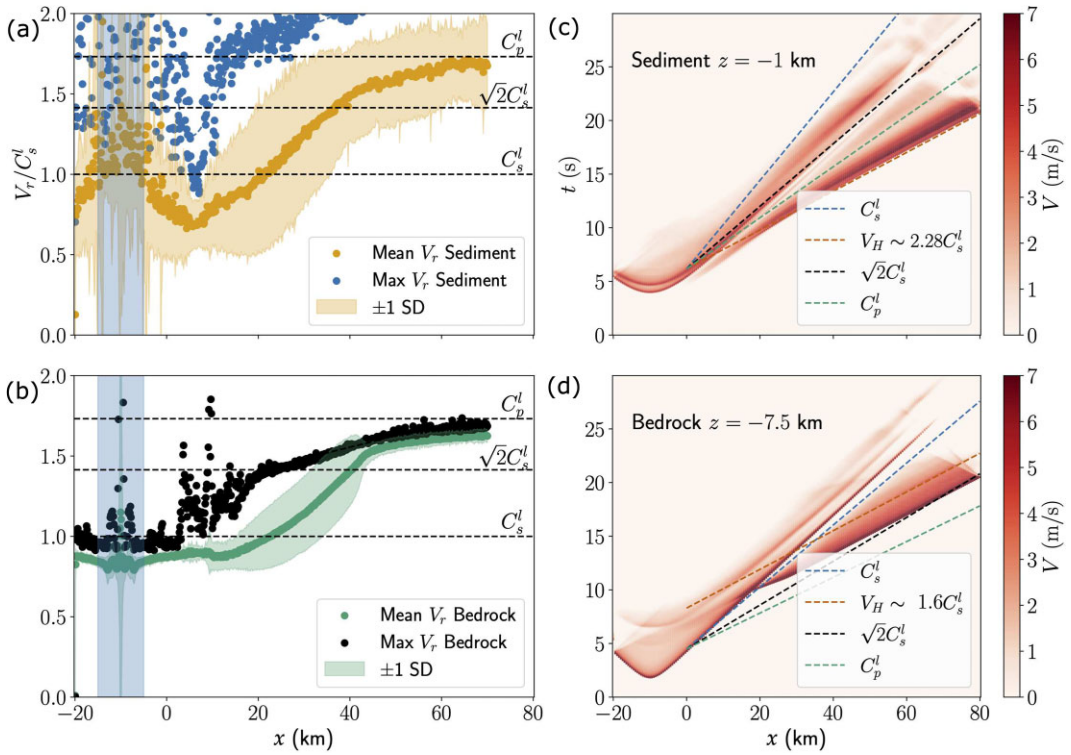

Figure 6. The rupture propagation speeds in Model A-2 (a–b) Mean and maximum rupture propagation speed V_r within both the sediment and the bedrock. The shaded area represents the nucleation site of the rupture. (c–d) Spatiotemporal slip rate distribution at depth 1 and 7.5 km, respectively, to highlight local horizontal propagation speed V_H relative to local characteristics speeds C_s^l, C_p^l and $\sqrt{2}C_s^l$.

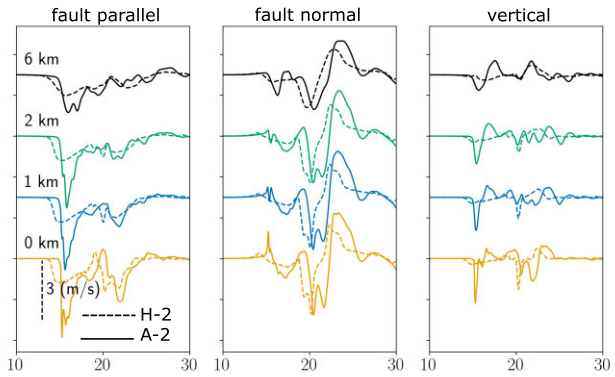

Figure 7. The role of sediment layer contrast in altering synthetic ground motion characteristics for Model A-2. (a) Fault-parallel (FP), (b) fault-normal (FN) and (c) vertical velocity time histories at four different sites. Sites are located at 50 km along strike and at distances (0^+, 1, 2, 6) along the fault perpendicular direction.

steady state is well justified by the fact that at later times (a) the rupture has fully saturated the seismogenic zone with no along-strike variations in stress, geometry or frictional properties, and (b) there is sufficient separation between the leading tip and the trailing one. We can then express the fault-normal velocity field during local supershear as Dunham (2005), Dunham & Archuleta (2005) and Mello *et al.* (2014b, 2016):

$$V_y = \mathcal{M}(\beta_s)\dot{\delta} = \frac{-1}{\beta_s}\left[\frac{1}{2} - \frac{1}{\beta_s^2 + 1}\right]\dot{\delta}. \tag{7}$$

In eq. (7), we separate the contributions of the slip rate and the rupture speed. Based on Fig. 6(c) and Fig. 3(c), the slip rate of the trailing Rayleigh is similar between models A-1 and A-2. Thus in order to understand the difference between Model A-1 and Model A-2, we need to examine how the term $\mathcal{M}$ varies between the two models. It is important to note that under those conditions the limit of $V_H \to \sqrt{2}C_s^l$, $\mathcal{M} \to 0$. This implies that as we approach Eshelby speed, the velocity pulse carried by the Mach cone in the fault-normal component should technically vanish.

In Model A-1, as shown in Fig. 3, the propagation speed of the slip pulse is sub-Eshelby ($V_H \sim 1.24$, $\beta_s = 0.733$). In Model A-2, the trailing rupture, that is propagating at locally supershear speed and carries the dominant fault-normal velocity pulse, accelerates towards the Eshelby speed ($V_H \sim 1.35$, $\beta_s = 0.91$). This increase in β_s, as the rupture accelerates, leads to a decrease in the magnitude of $\mathcal{M}$ and, consequently, the magnitude of the fault-normal velocity pulse carried by the Mach cone. This change is independent of the contribution of the slip rate which is similar between the two models. This observation highlights the importance of the changing rupture characteristics on near-fault ground motion.

3.2 Strong material contrast $C_s^1 = 0.5\,C_s^2$

3.2.1 Large fault strength ratio $\mathcal{S}_o = 3$ (B-1):

In Fig. 8 we show model B-1 with 50 per cent contrast to explore the role of increasing material contrast. We again start by exploring the large strength ratio case of $\mathcal{S}_o = 3$. We note that 50 per cent might be quite a large contrast for a 2 km deep

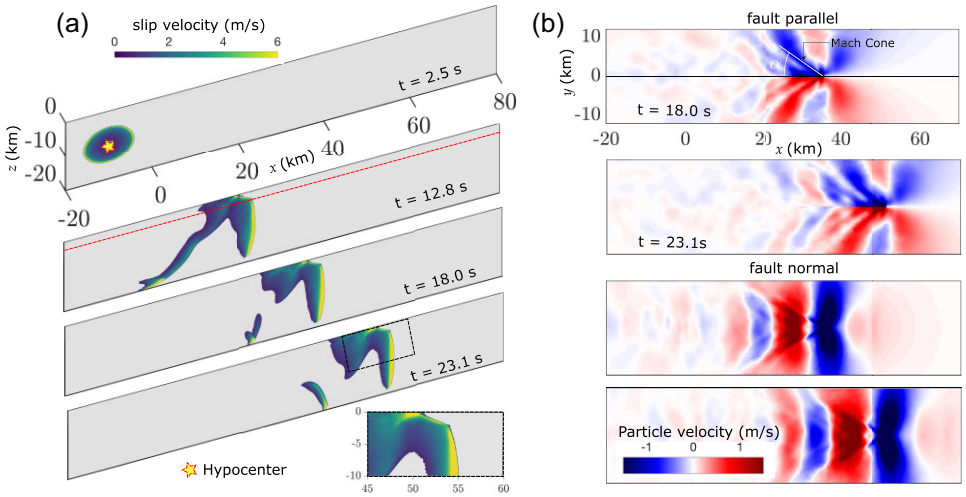

Figure 8. The role of sediment layer contrast in altering rupture propagation and ground motion characteristics for Model B-1. (a) snapshots of the rupture propagation at different times ($t = 2.5$, 12.8, 18.0 and 23.1 s). (b) Contours of the fault-parallel and fault-normal particle velocity wave-field within near field of the fault at later stages of rupture propagation ($t = 18.0$ s and $t = 23.1$ s).

shallow sediment. However, such high contrast would emphasize the potential differences when compared to the homogeneous case.

In Fig. 8(a) we show snapshots of the slip rate on the fault surface. In comparison with Model A-1, we observe similar rupture propagation characteristics with a minor difference in the orientation of the rupture front normal within the sediment (shown in zoomed-in panel Fig. 8a). This change is attributed to the softer sediment altering the curvature of the rupture front. The rupture propagation speed within the bedrock is still subshear, and it is the same as observed in Model A-1. Similar to Model A-1, we observe that the rupture front is still straight. To maintain this front geometry, the rupture tip consequently must propagate at the same horizontal rupture speed in both the sediment and the bedrock.

By examining the ground particle velocity wave-field in the near field of the fault shown in Fig. 8(b), we again observe the emergence of a Mach cone within the FP component. The Mach cone angle α is smaller than the one observed in Model A-1. Furthermore, the Mach cone also has a wider extent. From the ground particle velocity field, we estimate the Mach cone angle to be approximately $\alpha \sim 35^{\circ}$. Despite the rupture propagation speed at depth being the same in both Models A-1 and B-1, the structure of the Mach cone at the surface is different. This is due to the difference in propagation speeds relative to the local shear wave speed. Here, because of the larger contrast, there is a clear separation between the leading rupture tip and the reflections that emerge at the interface between the sediment and the bedrock. This separation leads to the emergence of a secondary pulse trailing the leading rupture tip. Furthermore, since the secondary pulse is also propagating at a speed faster than the local shear wave speed, it generates a Mach cone.

We examine the rupture propagation speeds in Fig. 9. In Fig. 9(a), we observe that the mean rupture speed V_r exceeds the local shear wave speed C_s^l in the distance range $x = 40$ to 70 km. Furthermore, the maximum V_r exceeds the local Eshelby speed. Within the bedrock, as shown in Fig. 9(b), the rupture propagation speed is subshear and is similar to Model A-1 shown in Fig. 3(b). The spatiotemporal evolution of the slip rate shows a similar pattern. The horizontal rupture propagation speed V_H exceeds the local Eshelby speed and is almost equal to the local pressure wave speed C_p^l, which coincides with the maximum value of V_r within the sediment. Within the bedrock, the propagation speed V_H is still subshear at $0.87C_s^l$. Similar to Model A-1, we can back-calculate the Mach cone angle using these rupture speed estimates. For $V_H = 1.73C_s^l$ in the sediment, the estimated Mach cone angle $\alpha = 35.3^{\circ}$, which is in agreement with the Mach cone angle observed in the particle velocity field.

Within the synthetic ground motion records shown in Fig. 10, we observe that the FP component jump becomes almost comparable to the FN component jump within the near-fault record 0^+. However, despite having a Mach cone angle lower than 45°, the FP is not the dominant component even at 0^+. Combined with the observations in Model A-1, *this implies that FN>FP jump may not rule out local supershear propagation. However, an FN>FP remains indicative of a dominant subshear propagation at depth.* We note here that, unlike global supershear rupture, there is no clear separation between the rupture tip and the trailing Rayleigh signature, which means that the ground motion signature is a superposition of a strong subshear component (at depth) and the local supershear effects (within the sediment), which would contribute to why the condition of FP>FN is not satisfied.

Furthermore, we observe secondary pulses in the FP component associated with the second Mach cone. Both FP pulses attenuate with fault perpendicular distance. Another important observation when comparing the role of material contrast is that despite a clear increase in contrast from Model A-1 to B-1, the increase in the contrast primarily affected the FP component with no apparent further amplification of the FN component. This is due to the competition between amplification by propagation through a softer material and dampening due to altered rupture propagation speed as discussed in the previous section.

3.2.2 *Small fault strength ratio $\mathcal{S}_o = 1.6$ (B-2)*

Similar to models A, we also explore a smaller initial fault strength ratio $\mathcal{S}_o$ to investigate the implications of having a sediment layer

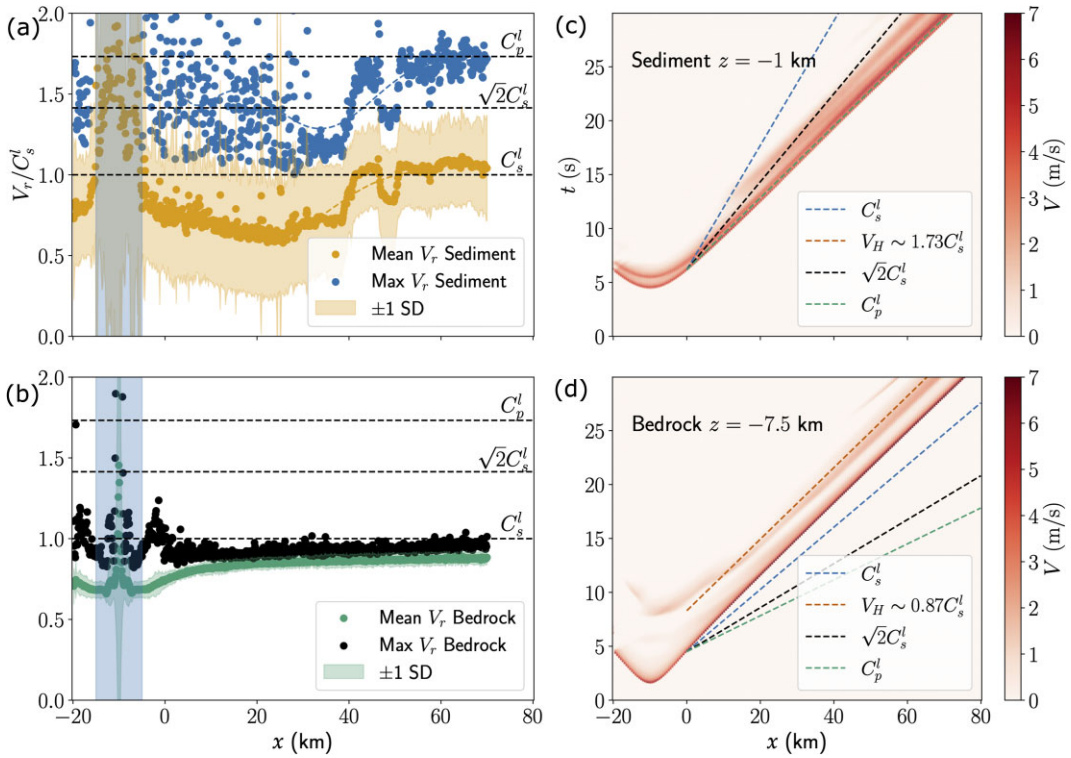

Figure 9. The rupture propagation speeds in Model B-1 (a–b) Mean and maximum rupture propagation speed V_r within both the sediment and the bedrock. The shaded area represents the nucleation site of the rupture. (c–d) Spatiotemporal slip rate distribution at depth 1 and 7.5 km, respectively, to highlight local horizontal propagation speed V_H relative to local characteristics speeds C_s^l, C_p^l and $\sqrt{2}C_s^l$.

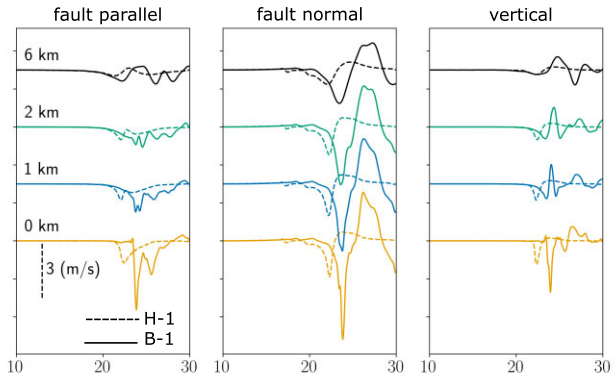

Figure 10. The role of sediment layer contrast in altering synthetic ground motion characteristics for Model B-1. (a) Fault-parallel (FP), (b) fault-normal (FN) and (c) vertical velocity time histories at four different sites. Sites are located at 50 km along strike and at distances (0^+, 1, 2, 6) along the fault perpendicular direction.

on global supershear propagation. We refer to this model as B-2. In Fig. 11(a) we again observe an earlier supershear transition relative to the homogeneous model for model B-2.

Within the velocity field, we see similar features to model A-2. However, due to the softer media, we observe the emergence of multiple Mach cones. The Mach cones' angles are different between the leading tip and the subsequent trailing signature. These Mach cones are associated with (1) local supershear propagation, and (2) reflected waves at the sediment-bedrock interface that now have sufficient separation between them due to the larger material contrast. We again emphasize that the velocity field carried by the rupture front is fault-parallel dominant.

The rupture propagation speed characteristics are shown in Fig. 12. We observe that the mean and maximum V_r within both the sediment and the bedrock exceed the Eshelby speed. Both the mean and the maximum V_r in the sediment exceed local pressure wave speed C_p^l. That is not the case for the bedrock as shown in Fig. 12(b), which is similar to Fig. 6(b) except for a delayed transition. The slip pulse propagation speeds V_H are estimated in Figs 12(c)–(d) to be $\sim 2.85C_s^l$ within the sediment and $\sim 1.6C_s^l$ within the bedrock. This apparent supersonic propagation is driven by the supershear rupture at depth and contributes to the complexity of the velocity field near the rupture tip.

Considering synthetic seismogram readings for Model B-2 shown in Fig. 13, we observe similar features to Model A-2, such as an initial large FP jump associated with the rupture tip passage, and then a second large FN jump associated with trailing Rayleigh. Within the FP component, we observe the influence of the multiple Mach cones which extend the large velocity pulse window prior to subsiding right before the trailing Rayleigh signature. The vertical component is also strongly amplified by the passage of the leading rupture tip.

3.3 Ground motion characteristics of subshear and supershear in the presence of sediments

In this section, we compare several key ground motion metrics for the following scenarios: (1) a subshear model $\mathcal{S}_o = 3$ with and without a sediment, and (2) a supershear model $\mathcal{S}_o = 1.3$. We set up these choices so that on average the rupture propagation is almost

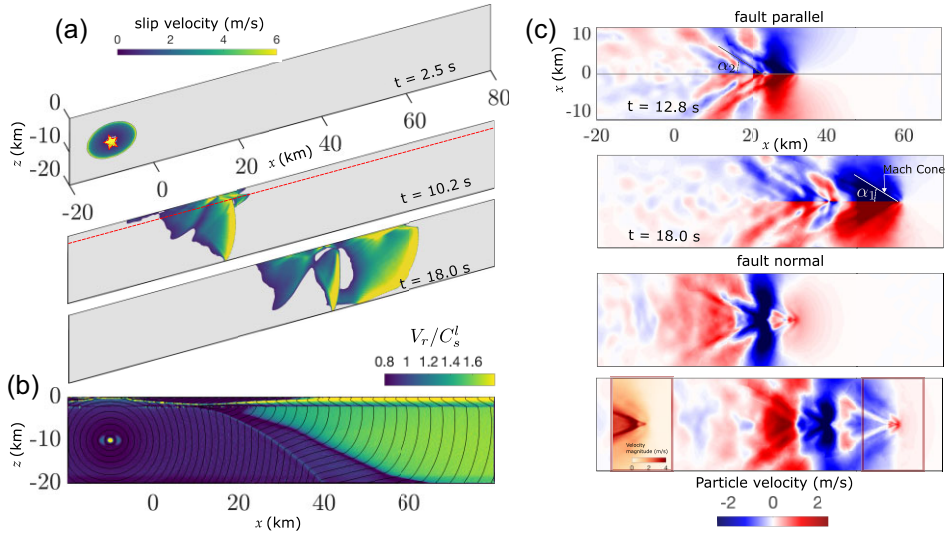

Figure 11. The role of sediment layer contrast in altering rupture propagation and ground motion characteristics for Model B-2. (a) snapshots of the rupture propagation at different times ($t = 2.5$, 10.2 and 18.0 s). (b) Contour of the normalized rupture speed V_r/C_s^l. (c) Contours of the fault-parallel and fault-normal particle velocity wave-field within near field of the fault at later stages of rupture propagation ($t = 12.8$ s and $t = 18.0$ s). Zoomed figure in last panel shows the particle velocity magnitude near the rupture tip at $t = 18.0$ s to highlight the structure of the Mach cone.

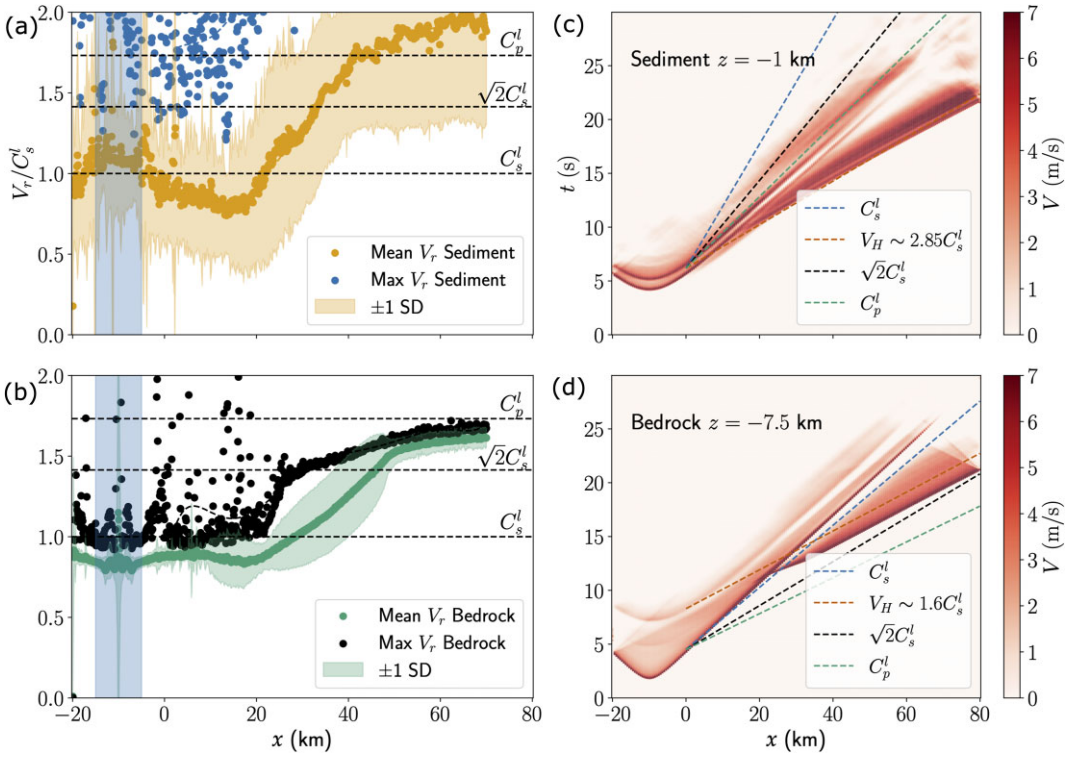

Figure 12. The rupture propagation speeds in Model B-2 (a–b) Mean and maximum rupture propagation speed V_r within both the sediment and the bedrock. The shaded area represents the nucleation site of the rupture. (c–d) Spatiotemporal slip rate distribution at depth 1 and 7.5 km, respectively, to highlight local horizontal propagation speed V_H relative to local characteristics speeds C_s^l, C_p^l and $\sqrt{2}C_s^l$.

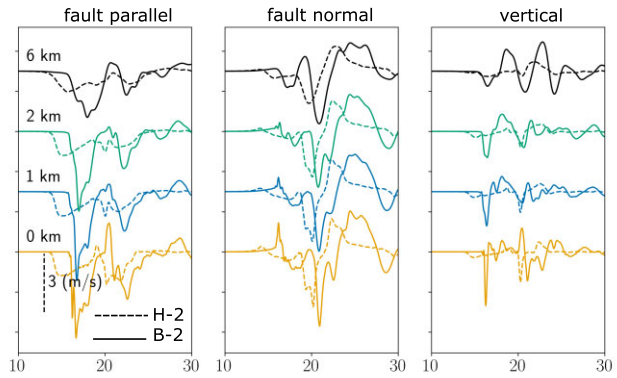

Figure 13. The role of sediment layer contrast in altering synthetic ground motion characteristics for Model B-2. (a) Fault-parallel (FP), (b) fault-normal (FN) and (c) vertical velocity time histories at four different sites. Sites are located at 50 km along strike and at distances (0^+, 1, 2, 6) along the fault perpendicular direction.

identical between the homogeneous and sediment models. The first scenario corresponds to models A-1, and H-1 (see Table 1) we showed earlier. The second scenario corresponds to models A-3, and H-3 and has a rapid transition to supershear rupture speed.

In Fig. 14, the orientation of peak ground velocity (PGV) is shown for the scenarios discussed earlier. In Figs 14(a) and (b) we observe that when the rupture is only propagating locally at supershear speeds, there is no difference in the orientation of PGV, as the amplification in the FP component is still not sufficient to exceed the FN component. This is consistent with our earlier observations that FN>FP does not necessarily exclude local supershear propagation. The distribution varies between the homogeneous model and the model with the sediment layer when the rupture is propagating globally at supershear speed as seen in Figs 14(c) and (d). We observe that, in the model with the sediment layer, the FP component becomes dominant sooner. This is attributed to the role of the soft layer and rupture acceleration in amplifying the FP component and attenuating the FN one.

In Fig. A5 we explore the amplification factors for PGV by comparing the homogeneous model with the sediment model. We show the ratio between PGV_S and PGV_H for each component, where subscripts S and H indicate the sediment model and the homogeneous model, respectively. We clearly see that the amplification of ground motion is heterogeneous within each individual component. In the fault-parallel direction, we observe that the PGV is amplified more near the fault at distances less than 5 km. This is explained by the nature of the local supersonic and supershear propagations amplifying the FP direction. Interestingly, we see that the FN component within the near-fault is not amplified but rather is decreased through the incorporation of sediment layers. However, this behaviour is confined to near-fault locations. As discussed earlier, because the rupture characteristics themselves are influenced by the incorporation of the sediment layer, we see that the amplification between the different components is also not uniform, with the FP PGV amplification being different from the FN PGV amplification.

In Fig. 15, we also examine the Fourier amplitude spectra (FAS) and spectral accelerations (PSa) for models with $S_o = 3$, at locations 1, 2, 5 km along the fault perpendicular direction, and 20, 30, 40 and 50 km along the strike. In general, as shown in Figs 15(a), (c), (e), (g), the model with the sediment layer (solid) has higher amplitudes than the homogeneous case (dashed). We also observe a higher frequency cut-off for models with the sediment layers in the near-fault region (1 and 2 km) versus their homogeneous counterparts. Within the spectral accelerations shown in Figs 15(b), (d), (f), (h), we observe generally larger peaks that shift towards smaller periods in the model with sediment layers. This observation is consistent with the higher cut-off frequency, which can potentially be explained by the emerging Mach cones from local supershear effects (Bizzarri & Spudich 2008). Furthermore, we observe that the decay of amplitude at higher frequency is larger for the sediment model compared to the homogeneous model. The differences in spectral accelerations between the homogeneous and sediment models highlight possible implications on the structural response of near-fault buildings and linear infrastructure that warrant further investigation.

Results for scenario 2 with $\mathcal{S}_o = 1.3$ are shown in Fig. 16. First, we observe that the FAS of both the homogeneous model and the sediment model are higher relative to scenario 1, which is consistent with the higher stress drop. We also observe that the decay of high-frequency content is different due to the nature of supershear attenuation. Similar to scenario 1, we observe that near-fault locations have a higher cut-off frequency before the decay of the FAS. Prior to supershear transition at $x = 20$ km, both the sediment model and the homogeneous model have similar spectral acceleration peak locations; however, after transition, the first peak of the amplitude curve occurs at smaller periods.

Overall, we observe a clear distinction between the frequency content for local supershear propagation and global supershear propagation. The models with sediment have a higher cut-off frequency and the peaks of the spectral accelerations occur at smaller periods. These observations highlight the importance of considering the role of sediments on rupture propagation and consequently the ground motion characteristics.

4 DISCUSSION

In this work, we examine the role of sediment layers on the ground motion characteristics of both supershear and subshear ruptures. We compare the results of models with sediment layers and models with homogeneous media with the same initial $\mathcal{S}$ parameter. In our analysis, we have utilized a simple one-layer model with a sharp interface to isolate the effects of the sediment. This assumption is an oversimplification based on field studies which highlight that velocity structure continues to vary with depth. Accordingly, we also model a 1-D linear velocity structure that is obtained from the East Anatolian fault zone (Güvercin *et al.* 2022) as a representative case. The material properties of this velocity structure are tabulated in Table A1. We refer to these models as LVS-1 and LVS-2. In Fig. A3(a) we show the particle velocity field in the FP and FN direction for a case with initial $\mathcal{S}_o = 3$. Similar to Model A-1, we observe the emergence of Mach cones at the free surface which are attributed to local supershear propagation. Further examining the synthetic seismograms and comparing with Model A-1, we observe almost identical features albeit with a small delay due to the different wave speed structure. We also explore differences in the limit that $\mathcal{S}_o = 1.6$, and while differences do emerge, the same qualitative features are preserved with Model A-2.

We have also assumed in our model that the frictional properties (a and b) are uniformly velocity-weakening until 15 km depth. This assumption might also be inconsistent with some laboratory experiments on rock friction at low normal stress, which suggest

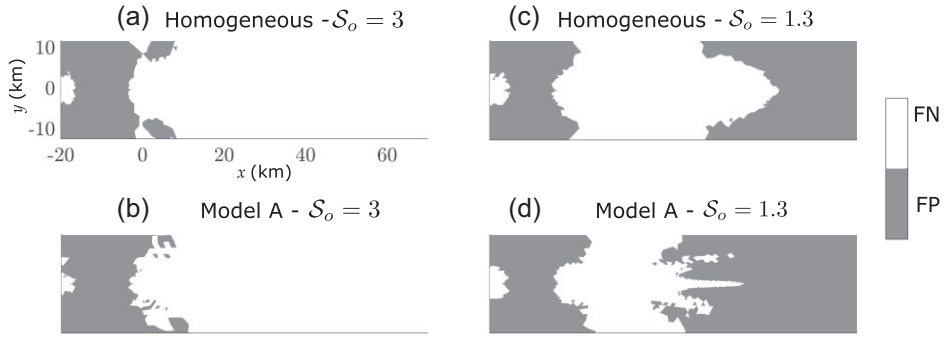

Figure 14. Orientation of the PGV for different scenarios with local supershear and global supershear comparing homogeneous models and sediment models. The maximum motion goes from predominantly fault-normal (white) to fault-parallel (grey).

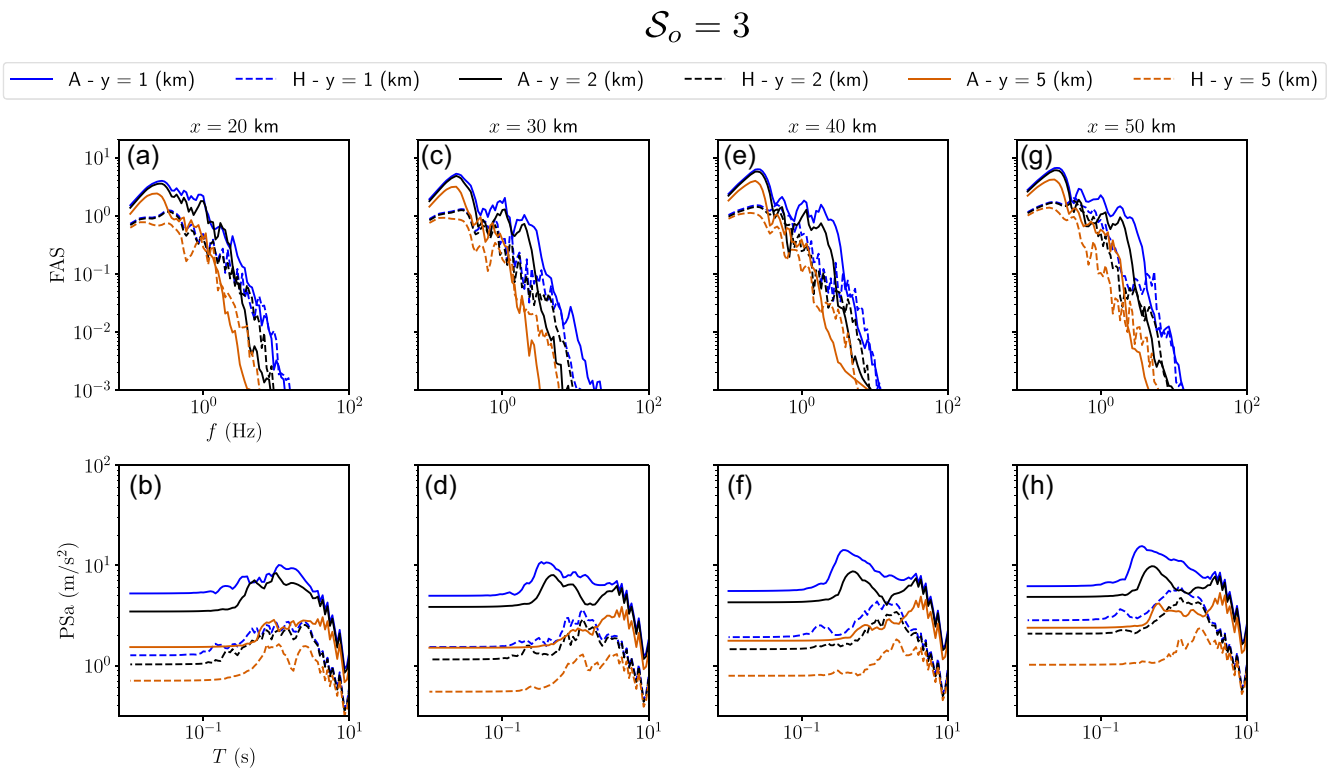

Figure 15. Ground motion metrics comparison between models with sediment and homogeneous models. The Fourier amplitude spectra (FSA) and the spectral accelerations (PSa) for a homogeneous model (dashed lines) and sediment model (solid lines) with an initial $\mathcal{S}_o = 3$. The site locations are 1, 2, 5 km along the fault perpendicular direction, and 20, 30, 40 and 50 km along the strike. The rupture propagation speed here is sub-shear for the homogeneous model and locally supershear for the sediment model.

a velocity-strengthening behaviour (Marone *et al.* 1991; Marone 1998). To account for this possibility, we further consider such variation in frictional properties by adding a velocity-strengthening patch near the free surface (coincident with low normal stress). In Figs A4(a)–(b) we show Models A-1^{VS} and A-2^{VS} which are equivalent to Model A-1 and A-2 with the only difference being the depth-dependent $(a - b)$. The variation in $(a - b)$ is chosen such that there is a linear increase in (a–b) from -0.004 at $d = 4$ km to 0.006 at $d = 0$ km. We note here that we retain the strong rate weakening behaviour even when the friction is velocity-strengthening. We observe qualitative agreement between models with and without shallow VS layer, with features such as local supershear and supersonic propagation diminished but still preserved. Accordingly, we expect that there is a parameter space in which a VS layer could diminish the extent of observed local effects. Furthermore, we also emphasize that in addition to a shallow layer with different frictional parameters, it is expected that during frictional sliding this shallow portion of bulk would

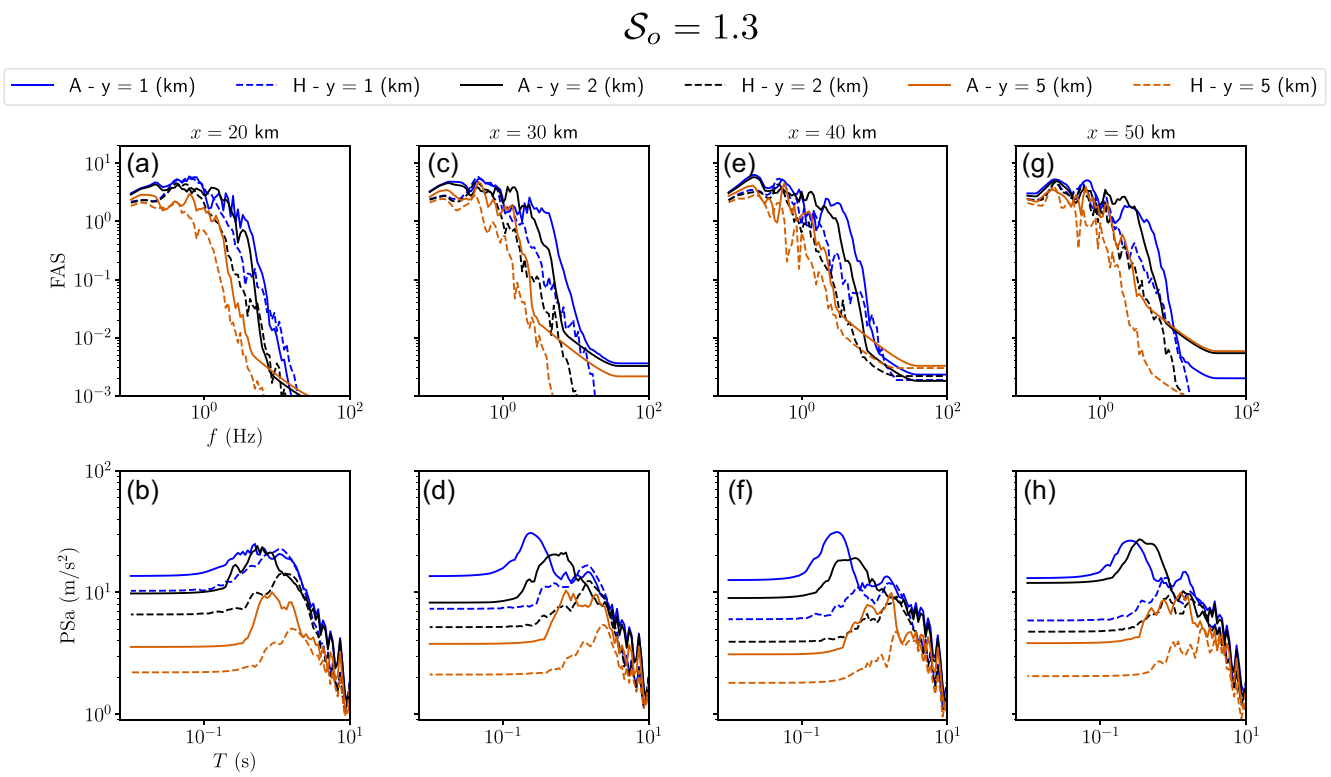

Figure 16. Ground motion metrics comparison between models with sediment and homogeneous models. The Fourier amplitude spectra (FSA) and the spectral accelerations (PSa) for a homogeneous model (dashed lines) and sediment model (solid lines) with an initial $\mathcal{S}_o = 1.3$. The site locations are 1, 2, 5 km along the fault perpendicular direction, and 20, 30, 40 and 50 km along the strike. The rupture propagation speed here is globally supershear for both the homogeneous and the sediment model.

experience damage accumulation, due to low mean stress, in the form of inelastic deformations. Inelastic deformations could provide sufficient dissipation to inhibit some of the features we observe in our models.

Furthermore, to explore the role of sediment thickness, in Figs A6 and A7 we represent the same models considered here with material contrast 70 per cent and 50 per cent but with sediment thickness of 5 km, respectively. To distinguish the different models, we refer to the models with thicker sediment layers by the same model's name but with a subscript $(*)$. In the larger thickness models, we observe an increase in the extent of supershear propagation within the fault surface. By examining the synthetic ground motion records for Model B-1*, we observe that despite rupture speed within the bedrock layer being subshear, the FP component of the near-fault (0^+, 1 km) records is comparable to that of the FN component. This implies that at larger sediment thickness we can indeed recover the FP>FN condition observed in the global supershear case. We explain this behaviour through the reduced influence of the subshear pulse on the free surface due to the increased depth of the sediment layer. Because of the altered rupture characteristics, we also observe that the amplitude of the FN leading pulse is smaller for Model B-1* than Model A-1* for near-fault stations (0^+, 1 and 2 km), which is unexpected given the softer material.

Another effect of the thickness is shown in Fig. A7. We observe that all Models with $\mathcal{S}_o = 1.6$ but one (Model B-2*) transitions to global supershear. Model B-2* features only local supershear propagation within the sediment layer while the rupture propagation speed within the bedrock remains subshear. In models A-2, B-2, we have shown that the presence of sediment promoted faster global supershear transition when compared to the homogeneous case, yet in Model B-2* the sediment suppresses the transition entirely. This observation of non-monotonicity can be attributed to both a large thickness and large contrast greatly limiting the P-SV conversion that leads to free surface induced supershear at that choice of $\mathcal{S}_o$.

In the models that feature supershear propagation within the sediment layer only (i.e. shallow supershear), we find that the FN particle velocity jump is larger than the FP particle velocity jump. This observation *implies that FN>FP does not rule out shallow supershear propagation*. Furthermore, in all our models with sediment layers that feature global supershear propagation (saturating the seismogenic zone), we find that FP particle velocity jump is larger than the FN particle velocity jump. This observation *implies that FP>FN is a sufficient condition for identifying supershear propagation when considering this form of sedimentary structure.* It remains to be seen under what conditions, if any, such observation might vanish for global supershear.

It is important to highlight that our models are all linearly elastic. At large slip velocity, which are likely to be observed with strong rate weakening friction, it is probable that the surrounding bulk would start to accumulate inelastic deformation. The partitioning of deformations between bulk inelasticity and fault slip could potentially alter some of the observations in this study such as the propagation speed and the transition to

supershear (Ben-Zion & Shi 2005; Preuss *et al.* 2020; Abdelmeguid *et al.* 2024). A potential future extension of this study would be to include Drucker-Prager like plasticity formulation (Dunham *et al.* 2011; Abdelmeguid & Elbanna 2022) or a continuum damage model (Lyakhovsky & Ben-Zion 2014; Lyakhovsky *et al.* 2016; Zhao *et al.* 2024) to study the implication of accumulating damage in sediment layers on the resultant ground motion characteristics.

Finally, we highlight that current methodologies of identifying earthquake rupture histories and consequently generating seismic hazard maps largely rely on kinematic inversion of the source properties. This is usually an ill-posed problem with large uncertainties due to source and path effects. This has been highlighted by the contradicting conclusions about the variability in rupture speed along the East Anatolian Fault in the recent 2023 February 6 Pazarcik Earthquake in Turkey, which happened to be well-instrumented. Theoretical models that can help constrain kinematic inversions are yet to mature to include realistic fault zone complexity. Now, with ever-increasing observational facilities, it is important to utilize realistic forward models to identify key characteristics of near-field ground motion records in the presence of realistic material heterogeneity to supplement inversion techniques and limit the degree of uncertainty. This will enable the scientific community to identify signatures within the ground motion records that will enable us to get rapid insights into the nature of the rupture propagation. These signatures can be utilized to constrain state-of-the-art kinematic inversion methods to better understand the rupture history. Such examples in which ground motion characteristics were used to identify rupture speeds already exist, such as in the cases of Denali and the M_w7.8 Turkey earthquakes (Dunham & Archuleta 2004a; Abdelmeguid *et al.* 2023; Rosakis *et al.* 2023).

5 CONCLUSIONS

Based on our study of ground motion characteristics of subshear and supershear ruptures in the presence of sediment layers, we draw the following conclusions:

(i) The existence of a sediment layer with lower wave-speeds may lead to local supershear propagation within the sediment while the propagation speed remains subshear in the bedrock. This results in the generation of Mach cones with a wide spectrum of angles based on the material contrast. This, in turn, enhances the ground shaking within the FP direction.

(ii) We find that the rupture propagation speed at the free surface (within the sediment) is coupled with the rupture propagation speed at depth, in models with sediment layers, despite the different material properties. This implies that it is possible to infer information about the rupture speed at depth based on surface measurements.

(iii) We find that FP>FN remains a sufficient condition to infer supershear propagation. However, we have found that supershear propagation in the shallow depth may be associated with FN>FP. Thus FN>FP may not rule out the possibility of local supershear propagation, but it remains indicative of dominant subshear propagation at depth.

(iv) We find that in models with the same rupture propagation speed (on average), the presence of sediment alters the ground motion characteristics significantly. In cases where the rupture is propagating globally at supershear speeds, we find that the sediment exclusively enhances the FP velocity pulse, while minimally changes the FN component. This leads to a PGV distribution that differs between the two models. We also find that sediment affects the frequency content of the ground motion, which would have implications on seismic hazard.

(v) We observe, in all models with sediment layer, a substantial enhancement in the fault vertical component of the ground velocity which would have important implications on hazard including applications related to the seismic demand on linear infrastructure and the generation of tsunami waves.

(vi) We find that sediment layers influence the generation of supershear propagation within the bedrock. For models A-2, A-2* and B-2 we find that sediment promotes global supershear. For model B-2* which features a larger sediment thickness, we observe that the sediment hinders the supershear transition. This non-monotonic behaviour highlights the importance of the sediment layer properties on free-surface-induced supershear transition.

These findings highlight the importance of considering heterogeneous subsurface material distribution in our physical models, as they may have significant implications on the source physics and the resulting ground motion characteristics. Our research provides new insights into the complex interactions between the sediment layers and the rupture dynamics. These findings are relevant for the continuous development of more robust seismic hazard assessments and for improving our understanding of earthquake processes in regions with sedimentary basins.

ACKNOWLEDGMENTS

We thank Editor Sidao Ni, Suli Yao and an anonymous reviewer for their insightful reviews that helped improve the manuscript. MA would like to thank Eric Dunham for insightful discussions. The authors would also like to thank Grigorios Lavrentiadis for sharing the scripts used to characterize the ground motion. AJR and MA acknowledges support by the Caltech/MCE Big Ideas Fund (BIF), as well as the Caltech Terrestrial Hazard Observation and Reporting Center (THOR). The simulations conducted in this study were possible thanks to the support of Amazon, through the AI4Science initiative. AE acknowledge support by the National Science Foundation CAREER award No. 1753249 for modelling complex fault zones. The authors acknowledge support from the Southern California Earthquake Center through a collaborative agreement between NSF. Grant Number: EAR0529922 and USGS. Grant Number: 07HQAG0008.

DATA AVAILABILITY

The software used to conduct the dynamic rupture model is open access and can be obtained at https://github.com/wqseis/drdg3d.

REFERENCES

Abdelmeguid, M. & Elbanna, A., 2022. Modeling sequences of earthquakes and aseismic slip (seas) in elasto-plastic fault zones with a hybrid finite element spectral boundary integral scheme, *J. geophys. Res.: Solid Earth,* **127**(12), e2022JB024548, doi:10.1029/2022JB024548.

Abdelmeguid, M., Zhao, C., Yalcinkaya, E., Gazetas, G., Elbanna, A. & Rosakis, A., 2023. Dynamics of episodic supershear in the 2023 m7. 8 kahramanmaraş/pazarcik earthquake, revealed by near-field records and computational modeling, *Commun. Earth Environ.,* **4**(1), 456, doi:10.1038/s43247-023-01131-7.

Abdelmeguid, M., Mia, M.S. & Elbanna, A., 2024. On the interplay between distributed bulk plasticity and local fault slip in evolving fault zone complexity, *Geophys. Res. Lett.,* **51,** e2023GL108060, doi:10.1029/2023GL108060.

Aki, K. & Richards, P.G., 2002. *Quantitative Seismology,* University Science Books.

Albertini, G. & Kammer, D.S., 2017. Off-fault heterogeneities promote supershear transition of dynamic mode ii cracks, *J. geophys. Res.: Solid Earth,* **122**(8), 6625–6641.

Andrews, D., 1976. Rupture velocity of plane strain shear cracks, *J. geophys. Res.,* **81**(32), 5679–5687.

Aochi, H., Durand, V. & Douglas, J., 2011. Influence of super-shear earthquake rupture models on simulated near-source ground motion from the 1999 Izmit, Turkey, earthquake, *Bull. seism. Soc. Am.,* **101**(2), 726–741.

Bao, H., Ampuero, J.-P., Meng, L., Fielding, E.J., Liang, C., Milliner, C.W., Feng, T. & Huang, H., 2019. Early and persistent supershear rupture of the 2018 magnitude 7.5 Palu earthquake, *Nat. Geosci.,* **12**(3), 200–205.

Bao, H., Xu, L., Meng, L., Ampuero, J.-P., Gao, L. & Zhang, H., 2022. Global frequency of oceanic and continental supershear earthquakes, *Nat. Geosci.,* **15**(11), 942–949.

Beeler, N., Tullis, T. & Goldsby, D., 2008. Constitutive relationships and physical basis of fault strength due to flash heating, *J. geophys. Res.: Solid Earth,* **113**(B1), doi:10.1029/2007JB004988.

Ben-Zion, Y. & Shi, Z., 2005. Dynamic rupture on a material interface with spontaneous generation of plastic strain in the bulk, *Earth planet. Sci. Lett.,* **236**(1-2), 486–496.

Bhat, H.S., Dmowska, R., Rice, J.R. & Kame, N., 2004. Dynamic slip transfer from the Denali to Totschunda Faults, Alaska: testing theory for fault branching, *Bull. seism. Soc. Am.,* **94**(6B), S202–S213.

Bizzarri, A. & Spudich, P., 2008. Effects of supershear rupture speed on the high-frequency content of s waves investigated using spontaneous dynamic rupture models and isochrone theory, *J. geophys. Res.: Solid Earth,* **113**(B5), doi:10.1029/2007JB005146.

Bouchon, M., Bouin, M.-P., Karabulut, H., Toksöz, M.N., Dietrich, M. & Rosakis, A.J., 2001. How fast is rupture during an earthquake? New insights from the 1999 Turkey Earthquakes, *Geophys. Res. Lett.,* **28**(14), 2723–2726.

Burridge, R., 1973. Admissible speeds for plane-strain self-similar shear cracks with friction but lacking cohesion, *J. geophys. Int.,* **35**(4), 439–455.

Christie-Blick, N. & Biddle, K.T., 1985. Deformation and basin formation along strike-slip faults, in *Strike-Slip Deformation, Basin Formation, and Sedimentation (Vol. 37),* pp. 1–34, eds, Biddle, K. T. & Christie-Blick, N., Society of Economic Paleontologists and Mineralogists.

Das, S. & Aki, K., 1977. A numerical study of two-dimensional spontaneous rupture propagation, *J. geophys. Int.,* **50**(3), 643–668.

Day, S.M., Graves, R., Bielak, J., Dreger, D., Larsen, S., Olsen, K.B., Pitarka, A. & Ramirez-Guzman, L., 2008. Model for basin effects on long-period response spectra in Southern California, *Earthq. Spectra,* **24**(1), 257–277.

Dieterich, J.H., 1979. Modeling of rock friction: 1. experimental results and constitutive equations, *J. geophys. Res.: Solid Earth,* **84**(B5), 2161–2168.

Duan, B., 2008. Effects of low-velocity fault zones on dynamic ruptures with nonelastic off-fault response, *Geophys. Res. Lett.,* **35**(4), doi:10.1029/2008GL033171.

Dunham, E.M., 2005, *The Dynamics and Near-Source Ground Motion of Supershear Earthquakes,* PhD thesis, University of California, Santa Barbara. Available at: https://pangea.stanford.edu/~edunham/publications/Dunham_thesis_05.pdf.

Dunham, E.M., 2007. Conditions governing the occurrence of supershear ruptures under slip-weakening friction, *J. geophys. Res.: Solid Earth,* **112**(B7), doi:10.1029/2006JB004717.

Dunham, E.M. & Archuleta, R.J., 2004a. Evidence for a supershear transient during the 2002 Denali fault earthquake, *Bull. seism. Soc. Am.,* **94**(6 SUPPL. B), 256–268.

Dunham, E.M. & Archuleta, R.J., 2004b. Evidence for a supershear transient during the 2002 denali fault earthquake, *Bull. seism. Soc. Am.,* **94**(6B), S256–S268.

Dunham, E.M. & Archuleta, R.J., 2005. Near-source ground motion from steady state dynamic rupture pulses, *Geophys. Res. Lett.,* **32**(3), doi:10.1029/2004GL021793.

Dunham, E.M., Belanger, D., Cong, L. & Kozdon, J.E., 2011. Earthquake ruptures with strongly rate-weakening friction and off-fault plasticity, part 1: Planar faults, *Bull. seism. Soc. Am.,* **101**(5), 2296–2307.

Ellsworth, W. *et al.*, 2004. Near-field ground motion of the 2002 Denali Fault, Alaska, earthquake recorded at pump station 10, *Earthq. Spectra,* **20**(3), 597–615.

Frankel, A., Stephenson, W. & Carver, D., 2009. Sedimentary basin effects in Seattle, Washington: ground-motion observations and 3D simulations, *Bull. seism. Soc. Am.,* **99**(3), 1579–1611.

Güvercin, S.E., Karabulut, H., Konca, A.O., Doğan, U. & Ergintav, S., 2022. Active seismotectonics of the East Anatolian Fault, *J. geophys. Int.,* **230**(1), 50–69.

Hirose, T. & Shimamoto, T., 2005. Growth of molten zone as a mechanism of slip weakening of simulated faults in Gabbro during frictional melting, *J. geophys. Res.: Solid Earth,* **110**(B5), doi:10.1029/2004JB003207.

Hu, F., Oglesby, D.D. & Chen, X., 2019. The sustainability of free-surface-induced supershear rupture on strike-slip faults, *Geophys. Res. Lett.,* **46**(16), 9537–9543.

Hu, F., Oglesby, D.D. & Chen, X., 2021. The effect of depth-dependent stress in controlling free-surface-induced supershear rupture on strike-slip faults, *J. geophys. Res.: Solid Earth,* **126**(5), e2020JB021459, 10.1029/2020JB021459.

Huang, Y. & Ampuero, J.-P., 2011. Pulse-like ruptures induced by low-velocity fault zones, *J. geophys. Res.: Solid Earth,* **116**(B12), doi:10.1029/2011JB008684.

Huang, Y., Ampuero, J.-P. & Helmberger, D.V., 2016. The potential for supershear earthquakes in damaged fault zones–theory and observations, *Earth planet. Sci. Lett.,* **433,** 109–115.

Ingersoll, R.V., 1988. Tectonics of sedimentary basins, *Geol. Soc. Am. Bull.,* **100**(11), 1704–1719.

Jemberie, A.L. & Langston, C.A., 2005. Site amplification, scattering, and intrinsic attenuation in the Mississippi embayment from coda waves, *Bull. seism. Soc. Am.,* **95**(5), 1716–1730.

Kaneko, Y. & Goto, H., 2022. The origin of large, long-period near-fault ground velocities during surface-breaking strike-slip earthquakes, *Geophys. Res. Lett.,* **49**(10), e2022GL098029, doi:10.1029/2022GL098029.

Kaneko, Y. & Lapusta, N., 2010a. Supershear transition due to a free surface in 3-D simulations of spontaneous dynamic rupture on vertical strike-slip faults, *Tectonophysics,* **493**(3-4), 272–284.

Kaneko, Y. & Lapusta, N., 2010b. Supershear transition due to a free surface in 3-D simulations of spontaneous dynamic rupture on vertical strike-slip faults, *Tectonophysics,* **493**(3–4), 272–284.

Lu, X., Rosakis, A.J. & Lapusta, N., 2010. Rupture modes in laboratory earthquakes: effect of fault prestress and nucleation conditions, *J. geophys. Res.: Solid Earth,* **115**(12), 1–25.

Lyakhovsky, V. & Ben-Zion, Y., 2014. Damage–breakage rheology model and solid-granular transition near brittle instability, *J. Mech. Phys. Solids,* **64,** 184–197.

Lyakhovsky, V., Ben-Zion, Y., Ilchev, A. & Mendecki, A., 2016. Dynamic rupture in a damage-breakage rheology model, *J. geophys. Int.,* **206**(2), 1126–1143.

Ma, X. & Elbanna, A., 2015. Effect of off-fault low-velocity elastic inclusions on supershear rupture dynamics, *J. geophys. Int.,* **203**(1), 664–677.

Marone, C., 1998. Laboratory-derived friction laws and their application to seismic faulting, *Annu. Rev. Earth Planet. Sci.,* **26**(1), 643–696.

Marone, C.J., Scholtz, C. & Bilham, R., 1991. On the mechanics of earthquake afterslip, *J. geophys. Res.: Solid Earth,* **96**(B5), 8441–8452.

Mello, M., Bhat, H., Rosakis, A. & Kanamori, H., 2010. Identifying the unique ground motion signatures of supershear earthquakes: theory and experiments, *Tectonophysics,* **493**(3–4), 297–326.

Mello, M., Bhat, H., Rosakis, A. & Kanamori, H., 2014a. Reproducing the supershear portion of the 2002 Denali earthquake rupture in laboratory, *Earth planet. Sci. Lett.,* **387,** 89–96.

Mello, M., Bhat, H.S., Rosakis, A.J. & Kanamori, H., 2014b. Reproducing the supershear portion of the 2002 Denali earthquake rupture in laboratory, *Earth planet. Sci. Lett.,* **387,** 89–96.

Mello, M., Bhat, H.S. & Rosakis, A.J., 2016. Spatiotemporal properties of sub-Rayleigh and supershear rupture velocity fields: theory and experiments, *J. Mech. Phys. Solids,* **93,** 153–181.

Preuss, S., Ampuero, J.P., Gerya, T. & van Dinther, Y., 2020. Characteristics of earthquake ruptures and dynamic off-fault deformation on propagating faults, *Solid Earth,* **11,** 1333–1360.

Rice, J.R. & Tse, S.T., 1986. Dynamic motion of a single degree of freedom system following a rate and state dependent friction law, *J. geophys. Res.: Solid Earth,* **91**(B1), 521–530.

Rosakis, A., Abdelmeguid, M. & Elbanna, A., 2023. Evidence of early supershear transition in the M_w 7.8 Kahramanmaraş earthquake from near-field records, preprint(arXiv:2302.07214).

Rosakis, A.J., Xia, K., Lykotrafitis, G. & Kanamori, H., 2007. Dynamic shear rupture in frictional interfaces: speeds, directionality, and modes, *Earthq. Seismol.,* **4,** 153–192.

Rubino, V., Rosakis, A. & Lapusta, N., 2017a. Understanding dynamic friction through spontaneously evolving laboratory earthquakes, *Nat. Commun.,* **8**(1), 15991, doi:10.1038/ncomms15991.

Rubino, V., Rosakis, A.J. & Lapusta, N., 2017b. Understanding dynamic friction through spontaneously evolving laboratory earthquakes, *Nat. Commun.,* **8**(May), 1–12.

Rubino, V., Rosakis, A.J. & Lapusta, N., 2020. Spatiotemporal properties of sub-Rayleigh and supershear ruptures inferred from full-field dynamic imaging of laboratory experiments, *J. geophys. Res.: Solid Earth,* **125**(2), 1–25.

Rubino, V., Tal, Y., Rosakis, A.J. & Lapusta, N., 2021. Evolution of dynamic shear strength of frictional interfaces during rapid normal stress variations, in *EPJ Web of Conferences,* Vol. **250,** p. 01016, eds, Gálvez, Francisco Gálvez Díaz-Rubio & David, Angel Cendón, EDP Sciences: Spain.

Rubino, V., Lapusta, N. & Rosakis, A., 2022. Intermittent lab earthquakes in dynamically weakening fault gouge, *Nature,* **606**(7916), 922–929.

Ruina, A., 1983. Slip instability and state variable friction laws, *J. geophys. Res.: Solid Earth,* **88**(B12), 10 359–10 370.

Shlomai, H., Adda-Bedia, M., Arias, R. & Fineberg, J., 2020. Supershear frictional ruptures along bimaterial interfaces, *J. geophys. Res.: Solid Earth,* **125**(8), e2020JB019829, doi:10.1029/2020JB019829.

Song, S.G., Beroza, G.C. & Segall, P., 2008. A unified source model for the 1906 San Francisco earthquake, *Bull. seism. Soc. Am.,* **98**(2), 823–831.

Tal, Y., Rubino, V., Rosakis, A.J. & Lapusta, N., 2020. Illuminating the physics of dynamic friction through laboratory earthquakes on thrust faults, *Proc. Natl Acad. Sci.,* **117**(35), 21 095–21 100.

Tsutsumi, A. & Shimamoto, T., 1997. High-velocity frictional properties of gabbro, *Geophys. Res. Lett.,* **24**(6), 699–702.

Vyas, J.C., Mai, P.M., Galis, M., Dunham, E.M. & Imperatori, W., 2018. Mach wave properties in the presence of source and medium heterogeneity, *J. geophys. Int.,* **214**(3), 2035–2052.

Walker, K.T. & Shearer, P.M., 2009. Illuminating the near-sonic rupture velocities of the intracontinental kokoxili M_w 7.8 and denali fault M_w 7.9 strike-slip earthquakes with global *P* wave back projection imaging, *J. geophys. Res.: Solid Earth,* **114**(B2). doi:10.1029/2008JB005738.

Weng, H. & Ampuero, J.-P., 2020. Continuum of earthquake rupture speeds enabled by oblique slip, *Nat. Geosci.,* **13**(12), 817–821.

Xia, K., Rosakis, A.J. & Kanamori, H., 2004. Laboratory earthquakes: the sub-Rayleigh-to-supershear rupture transition, *Science,* **303**(5665), 1859–1861.

Xia, K., Rosakis, A.J., Kanamori, H. & Rice, J.R., 2005. Laboratory earthquakes along inhomogeneous faults: directionality and supershear, *Science,* **308**(5722), 681–684.

Xu, J., Chen, X., Liu, P. & Zhang, Z., 2020. Ground motion signatures of supershear ruptures in the Burridge-Andrews and free-surface-induced mechanisms, *Tectonophysics,* **791,** 228570, doi:10.1016/j.tecto.2020.228570.

Xu, J., Zhang, Z. & Chen, X., 2021. The effects of sediments on supershear rupture, *Tectonophysics,* **805,** 228777, doi:10.1016/j.tecto.2021.228777.

Zeng, H., Wei, S. & Rosakis, A., 2022. A travel-time path calibration strategy for back-projection of large earthquakes and its application and validation through the segmented super-shear rupture imaging of the 2002 M_w 7.9 Denali earthquake, *J. geophys. Res.: Solid Earth,* **127**(6), e2022JB024359, doi:10.1029/2022JB024359.

Zhang, W., Liu, Y. & Chen, X., 2023. A mixed-flux-based nodal discontinuous Galerkin method for 3D dynamic rupture modeling, *J. geophys. Res.: Solid Earth,* **128,** e2022JB025817, doi:10.1029/2022JB025817.

Zhao, C., Mia, M.S., Elbanna, A. & Yehuda, B.-Z., 2024. Dynamic rupture modeling in a complex fault zone with distributed and localized damage, *Mech. Mater.,* **,198,** 105139, doi:10.1016/j.mechmat.2024.105139.

APPENDIX A: SUPPLEMENTARY FIGURES

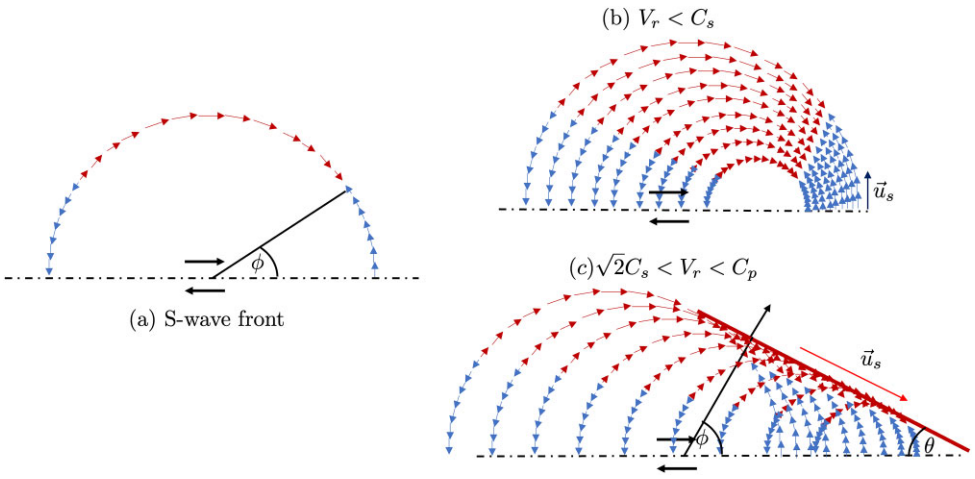

Figure A1. Geometric characteristics of subshear and supershear (super-Eshelby) propagation.

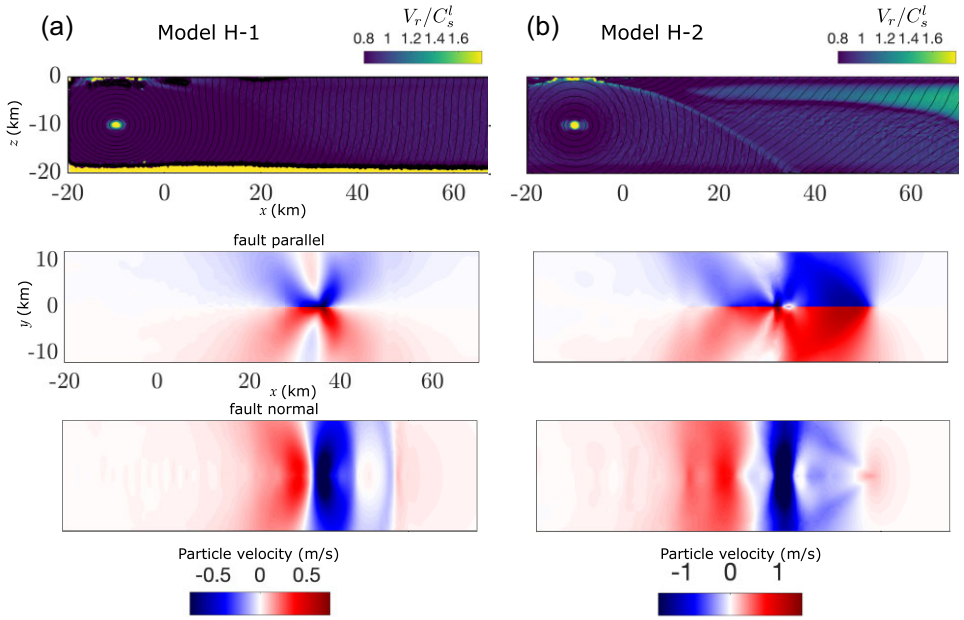

Figure A2. Reference homogeneous models H-1 and H-2. (A) Model H-1 with $\mathcal{S}_o = 3$. Top panel showing the normalized rupture propagation speed which is subshear. Bottom panel showing the signature subshear near-fault velocity wave-field. (B) Model H-2 with $\mathcal{S}_o = 1.6$. Top panel showing the normalized rupture propagation speed and supershear transition. Bottom panel showing the Mach cone generation in the near-fault velocity wave-field.

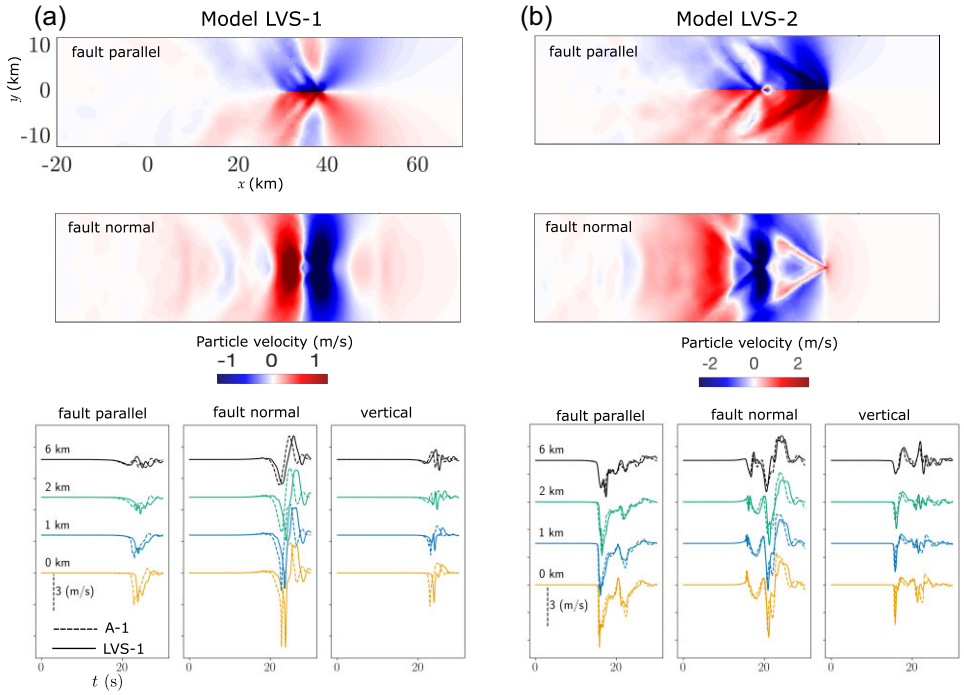

Figure A3. Models with linear velocity structure (LVS). (A–B) Model LVS-1 with $\mathcal{S}_o = 3$ and Model LVS-2 with $\mathcal{S}_o = 1.6$. Top panel showing the the near-fault velocity wave-field which is very similar to model A-1. Bottom panel showing the Fault-parallel (FP), fault-normal (FN) and vertical velocity time histories at four different sites. Sites are located at 50 km along strike and at distances (0^+, 1, 2, 6) km along the fault perpendicular direction. The ground motion is a slightly delayed version of model A-1 due to different wave speeds.

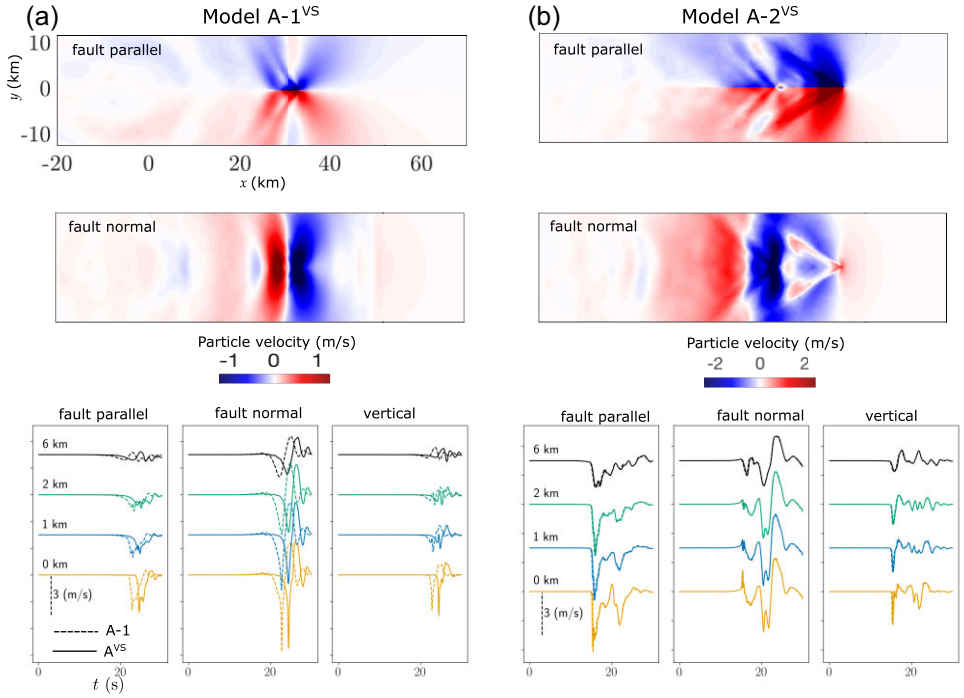

Figure A4. Models with a velocity-strengthening shallow layer. (A–B) Model A-1^{VS} with $\mathcal{S}_o = 3$ and Model A-2^{VS} with $\mathcal{S}_o = 1.6$. Top panel showing the the near-fault velocity wave-field which is very similar to model A-1. Bottom panel showing the Fault-parallel (FP), fault-normal (FN) and vertical velocity time histories at four different sites. Sites are located at 50 km along strike and at distances (0^+, 1, 2, 6) km along the fault perpendicular direction. The ground motion is a slightly delayed version of model A-1 due to different wave-speeds. In order to have a velocity-strengthening behaviour, the value of $(a - b)$ increases linearly to 0.006 as we approach the free surface.

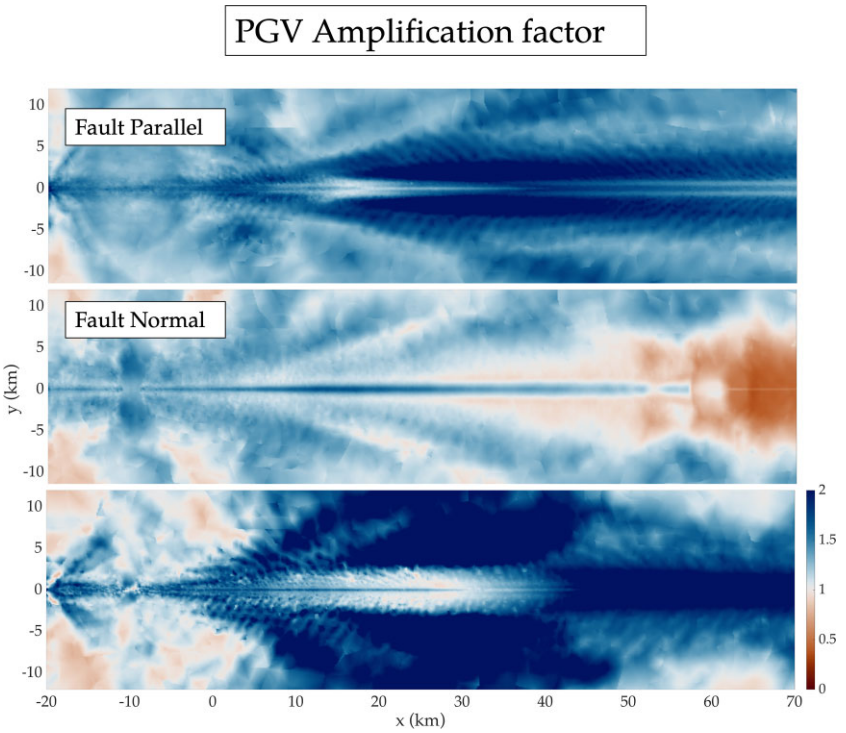

Figure A5. The amplification and dampening of the PGV components (fault-parallel, fault-normal and vertical). The contour colours show the ratio between the PGV of model A-3 and PGV model H-3.

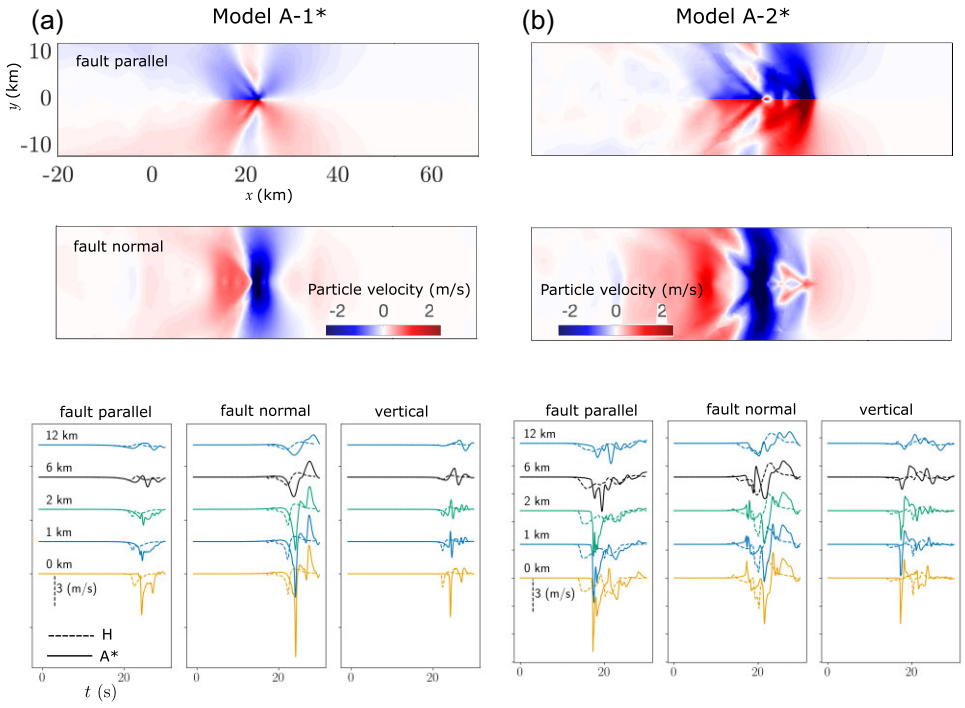

Figure A6. Models A (mild material contrast) with a 5 km thick sediment layer. (A–B) Model A-1* with $\mathcal{S}_o = 3$ and Model A-2* with $\mathcal{S}_o = 1.6$. Top panel showing the the near-fault velocity wave field which is very similar to model A-1. Bottom panel showing the Fault-parallel (FP), fault-normal (FN) and vertical velocity time histories at five different sites. Sites are located at 50 km along strike and at distances (0^+, 1, 2, 6, 12) km along the fault perpendicular direction.

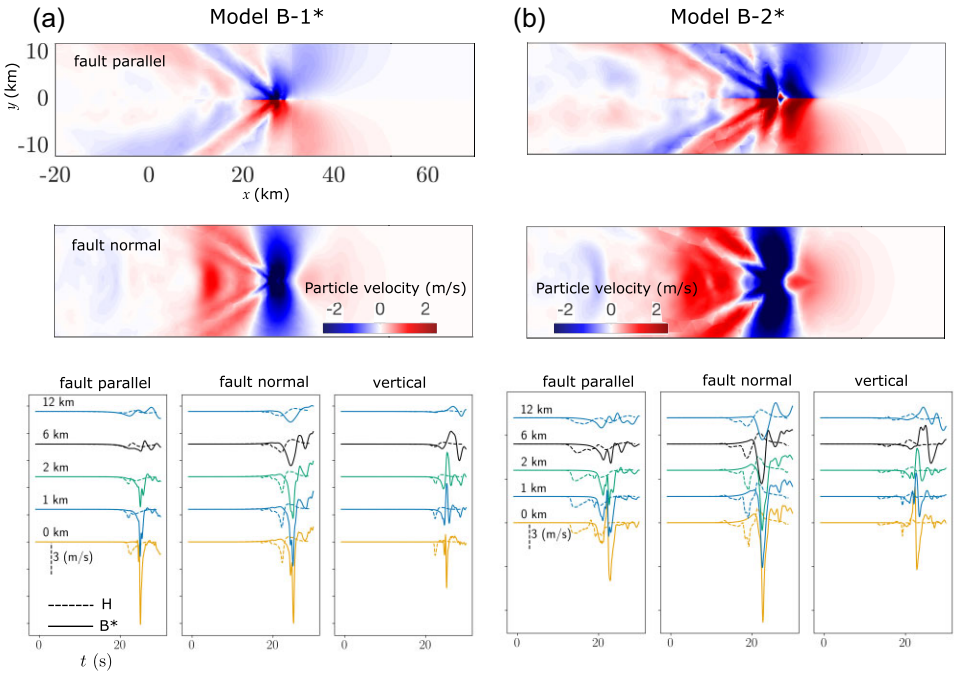

Figure A7. Models B (strong material contrast) with a 5 km thick sediment layer. (A–B) Model B-1* with $\mathcal{S}_o = 3$ and Model B-2* with $\mathcal{S}_o = 1.6$. Top panel showing the near-fault velocity wave field which is very similar to model A-1. Bottom panel showing the Fault-parallel (FP), fault-normal (FN) and vertical velocity time histories at five different sites. Sites are located at 50 km along strike and at distances (0^+, 1, 2, 6, 12) km along the fault perpendicular direction.

Table A1. The 1-D linear velocity model used in this study based on studies of the East Anatolian Fault (EAF) zone (Güvercin *et al.* 2022).

Depth (km)	C_p **(km s^{-1})**	C_s **(km s^{-1})**
0	3.88	2.04
1	4.52	2.43
2	5.62	3.03
4	5.75	3.31
6	5.85	3.38
8	5.96	3.43
10	6.00	3.44
12	6.05	3.46
16	6.32	3.62
20	6.40	3.67